The Pennsylvania State University

The Graduate School

Department of Electrical Engineering

TIME-FREQUENCY SIGNAL PROCESSING

TECHNIQUES FOR RADAR REMOTE SENSING

A Thesis in

Electrical Engineering

by

Chun-Hsien Wen

Submitted in Partial Fulfillment
of the Requirements
for the Degree of

Doctor of Philosophy

May 2005

The thesis of Chun-Hsien Wen was reviewed and approved* by the following:

John F. Doherty
Associate Professor of Electrical Engineering
Thesis Adviser
Chair of Committee

John D. Mathews
Professor of Electrical Engineering

Victor Pasko
Associate Professor of Electrical Engineering

Aleksander Wolszczan
Evan Pugh Professor of Astronomy and Astrophysics

W. Kenneth Jenkins
Professor of Electrical Engineering
Head of the Department of Electrical Engineering

*Signatures are on file in the Graduate School

Abstract

The Arecibo 430 MHz Incoherent Scatter Radar (ISR) has been used to observe the vertical ionospheric electron concentration profiles for many years. Earlier studies are dated back to 1970s. The meteor observations grew from the ISR observations of the ionosphere in the last 10 years. The techniques for meteor observation have evolved significantly since then. It has become a regular observation at Arecibo Observatory (AO). In this work we introduce signal processing techniques to detect meteor events and determine their parameters for the meteor observation data. We also propose techniques to separate the meteor and the incoherent scatter signals for the ISR observation data.

The large aperture AO radar is susceptible to the interference from other communication systems because of its sensitivity. The interference contaminates the radar data and sometimes seriously degrades the performance of the meteor detection. We introduce signal processing techniques to remove the interference for both the meteor and the ISR observation data in this work. Other applications for proposed techniques are introduced in this work too.

Table of Contents

List of Figures

Acknowledgments

This effort was supported under NSF Grants ATM-0113454 and AST-0205848 to The Pennsylvania State University. The Arecibo Observatory is part of the National Astronomy and Ionosphere Center which is operated by Cornell University under cooperative agreement with the National Science Foundation. As always we thank the Arecibo staff for their efforts.

I would like to express my appreciation to Dr. John F. Doherty and Dr. John D. Mathews for their helpful comments and the excellent research environment they provide; and my committee members, Dr. Victor Pasko and Dr. Aleksander Wolszczan, for their opinions about my thesis.

I also want to take this opportunity to express a special thank to my wife, my parents and my older brother for their support and encouragement for so many years. Without them I won't be able to finish my work.

To My Wife and Parents

Chapter 1

Introduction

1.1 Meteor Observation

Meteor observation using the 430 MHz incoherent scatter radar (ISR) of Arecibo Observatory (AO) was first introduced by the authors of [1]. Subsequently the authors of [2, 3, 4, 5, 6] reported the studies of the properties of the meteors. Currently the meteor observation are made by using 45-μs carrier pulses with an inter-pulse period (IPP) of 1-ms. The return signals are demodulated in in-phase and quadrature-phase channels and sampled at a 1- μs^{-1} rate.

The high power, large aperture AO radar permits us to directly measure the Doppler velocities of the meteor head echo. Previous works [4, 7] showed that the Doppler speed can be accurately determined by using the autocorrelation function of the return signal. With accurate meteor speed, other parameters of the meteor, such as meteor orbit, can be determined [2]. There are some inherent limitations of the method mentioned above. The similarity of the autocorrelation functions for both elemental incoherent scatter and meteor returns results in poor detection performance for autocorrelation-based methods. In this work, we introduce new signal processing techniques [5, 8] to detect meteors, which provide very precise Doppler speed estimates even for very low signal-to-noise ratio (SNR) meteor return signals. Two methods are investigated. First, we use a first-in-first-out (FIFO) FFT to detect the meteor. Second,

we construct a filterbank to detect the energy of different Doppler frequency components. When the energy exceeds a certain threshold, we declare meteor detection.

Because of the high sensitivity of the AO radar, it is susceptible to interference from other communication systems. The interference observed in AO meteor data is usually non-periodic and bursty. It seriously degrades the meteor detection performance. To alleviate this problem, we detect and remove the interference prior to the meteor detection process [9]. We calculate the central moments and apply a nonlinear filter to get the power reduction percentage of the power profile of each IPP signal. We then use these two parameters to identify the presence of the interference and then blank the corresponding signal samples.

1.2 Ionosphere Observation

The incoherent scatter radar (ISR) located at Arecibo has been used to observe the vertical ionospheric electron concentration profiles for many years. Earlier studies of E region ion layers at Arecibo include [10, 11, 12], and recent studies include [13, 14, 15].

Currently the ISR ionosphere observations are made using 13-baud Barker or 88-baud pseudo-random coded pulses. The meteor returns seen in the so-called ISR power-profile results are often spread over twice the code length as the meteor return voltages are incorrectly decoded due to significant Doppler offsets. The range-spread meteor return then contaminates the ISR power-profile effectively found by squaring and adding – in practice, all processing is done in the transform domain via FFTs. Here we separate ISR and meteor returns using Doppler filters in a manner that preserves

maximal information in both signal paths. We describe the design of specific filters to separate the signals based on the inherent differences between the incoherent scatter and meteor signals to separate the signals. For the ISR ionosphere observation data, we use a filterbank followed by the short time Fourier transform (STFT) analysis to remove the meteor signals. [16] introduced similar technique for meteor head-echo observations using 13 baud Barker code. We also analyze the separated meteor signals thus providing useful information for the meteor head-echo research.

1.3 Contribution to Knowledge

We introduce signal processing techniques for the meteor detection and the interference removal for both AO meteor observation data and ISR observation data. We prove that we can detect very weak meteor events using our techniques. Experimental results show that we detect about 20% more meteor events comparing to the traditional method [4, 7]. Also the whole meteor detection and interference removal processes are done by automated fashion, which saves us a lot of processing time.

1.4 Organization of the Thesis

Chapter 2 introduces the meteor detection and the separation of meteor and incoherent scatter signals algorithms for meteor observation data. The interference detection and removal process for meteor observation data is described in Chapter 3. Chapter 4 introduces signal processing techniques for ionosphere observation data including the algorithm to separate the meteor and incoherent scatter signals and

interference removal. Chapter 5 describes some applications using the proposed techniques. Conclusions and future works are given in Chapter 6.

1.5 Publications for this work

Journal publication

1. J. D. Mathews, J. F. Doherty, C.-H. Wen, S. J. Briczinski, D. Janches, D. D. Meisel, "An update of UHF radar meteor observations and associated signal processing techniques at Arecibo Observatory," *Journal of Atmospheric and Solar-Terrestrial Physics*, Vol. 65, pp. 1139-1149, July 2003.
2. C.-H. Wen, J. F. Doherty, J. D. Mathews, "Time-frequency radar processing for meteor detection," *IEEE Trans. Geosci. Remote Sensing*, *IEEE Trans*., Vol. 42, Issue 3, 501-510, March 2004.
3. C.-H. Wen, J. F. Doherty, J. D. Mathews, "Adaptive Filtering for the Separation of Incoherent Scatter and Meteor Signals for Arecibo Observation Data," *Journal of Atmospheric and Solar-Terrestrial Physics*, in press.
4. C. .-H. Wen, J. F. Doherty, J. D. Mathews, D. Janches, "Meteor detection and non-periodic bursty interference removal for Arecibo data," *Journal of Atmospheric and Solar-Terrestrial Physics,* Vol. 67, pp. 275-281, February 2005

Conference paper

1. C.-H. Wen, J. F. Doherty, J. D. Mathews, "Signal processing for meteor detection from Arecibo observatory data," Coupling, Energetics and Dynamics of Atmospheric Regions workshop, June 2002

2. Mathews, J.D., J. Doherty, C.-H. Wen, D. Janches, and D.D. Meisel, Meteor science issues addressed via UHF radar meteor observations at Arecibo Observatory, *Asteroids, Comets, & Meteors*, Berlin, Germany, Poster, 4-23, 29 July - 2 August, 2002
3. Mathews, J.D., J. Doherty, C.-H. Wen, D. Janches, and D.D. Meisel, Meteor science issues addressed via UHF radar meteor observations at Arecibo Observatory, in *Proceedings of Asteroids, Comets, & Meteors (ACM 2002)*, edited by B. Warmbein, pp. 253-256, European Space Agency, Berlin, Germany, 2002
4. C.-H. Wen, J. F. Doherty, J. D. Mathews, "Signal processing for bursty interference removal from Arecibo observatory data," Coupling, Energetics and Dynamics of Atmospheric Regions workshop, June 2003
5. Briczinski, S.J., J.D. Mathews, C.-H. Wen, and J.F. Doherty, Observations of sporadic meteor events using the 430 MHz Arecibo Observatory radar, *CEDAR Workshop*, Longmont CO, poster, 2003
6. C.-H. Wen, J. F. Doherty, J. D. Mathews, "On the Search of HyperSpeed Meteor," Coupling, Energetics and Dynamics of Atmospheric Regions workshop, June 2004
7. C.-H Wen, J. F. Doherty, J. D. Mathews, "A Report on Current Research Regarding the Meteor Trail Echo and Hyper-Speed Meteor Events Using the Arecibo 430 MHz Radar," National Radio Science Meeting, January 2005

Chapter 2

Meteor Detection

In this chapter, we present signal processing techniques to detect meteor returns from AO observation data. We exploit the characteristics of the transmit waveform in frequency domain as well as in time domain. Two detection methods are investigated. First, when a meteor is present in the radar return over several inter-pulse periods, there will be a periodic structure in frequency spectrum. By detecting this structure, we detect the presence of a meteor. Second, we construct a matched filterbank to detect the energy of different Doppler frequency components. When the energy exceeds a certain threshold, we declare meteor detection. We find the altitude of a meteor by finding the peak of the matched filter output. We also introduce the short time Fourier transform (STFT) analysis and the least mean square (LMS) adaptive filter to improve the detection performance and remove the incoherent scatter signals, respectively.

We model the meteor return signal in Section I. Frequency and time domain detection methods are introduced in Section II and Section III, respectively. Section IV and V introduce the STFT analysis and the LMS adaptive filter, respectively. Experimental results are given in Section VI.

2.1 Meteor Return Signal Model

Given the transmission of a 45-μs pulse, the meteor return signal is also 45-μs long with a corresponding Doppler frequency. With the 1-μs^{-1} sampling rate, we have

45 samples of the meteor return signal. We model the sampled, noise-free return signal as

$$m[n] = A\exp\left\{ j\left(\omega_D n + \phi\right)\right\}\Delta\left[n - l_M\right],\ n = 1, 2, ..., N_{IPP} \tag{2.1}$$

where A is the amplitude, ω_D is Doppler frequency, ϕ is the phase, l_M is the location of the meteor, N_{IPP} is the number of samples in one IPP, and $\Delta\left[n\right]$ is expressed as

$$\Delta\left[n\right] = u\left[n\right] - u\left[n - 44\right] \tag{2.2}$$

where $u\left[n\right]$ is the unit step function.

Fig. 2.1 shows the images of a relatively intense meteor event recorded at 07:37:39.704 AST 24 February 2001, which serves as an illustration of the types of signals we encounter. The image consists of 160 IPPs. Each IPP has 250 signal samples ($N_{IPP} = 250$). The glints of background noise are caused by elemental incoherent scatter [5]. We will use this event as a prototype to explain our detection methods. Fig. 2.2 shows the meteor return signal of IPP #85 of the prototype meteor event in Fig. 2.1, which matches our model.

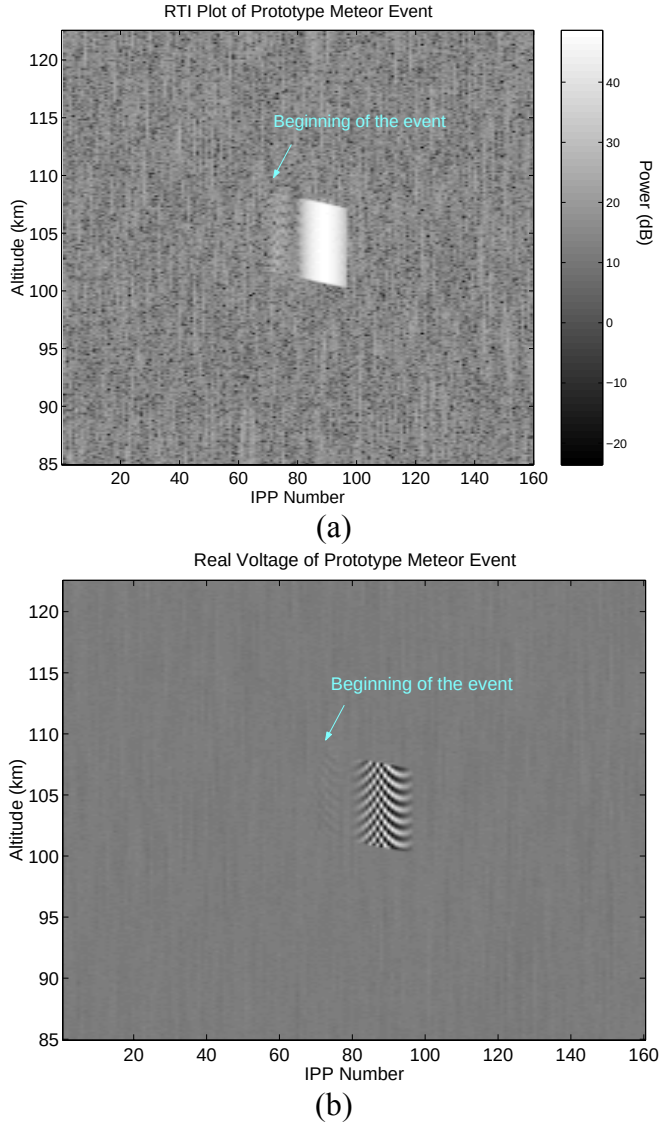

Figure 2.1: Prototype meteor event (a) Range-Time-Intensity (RTI) plot of the prototype meteor event. There are 160 IPPs in this image. Each IPP has 250 signal samples. (b) Real part of complex voltage of the prototype meteor event. This is a 26-IPP long meteor event from IPP #69~#95.

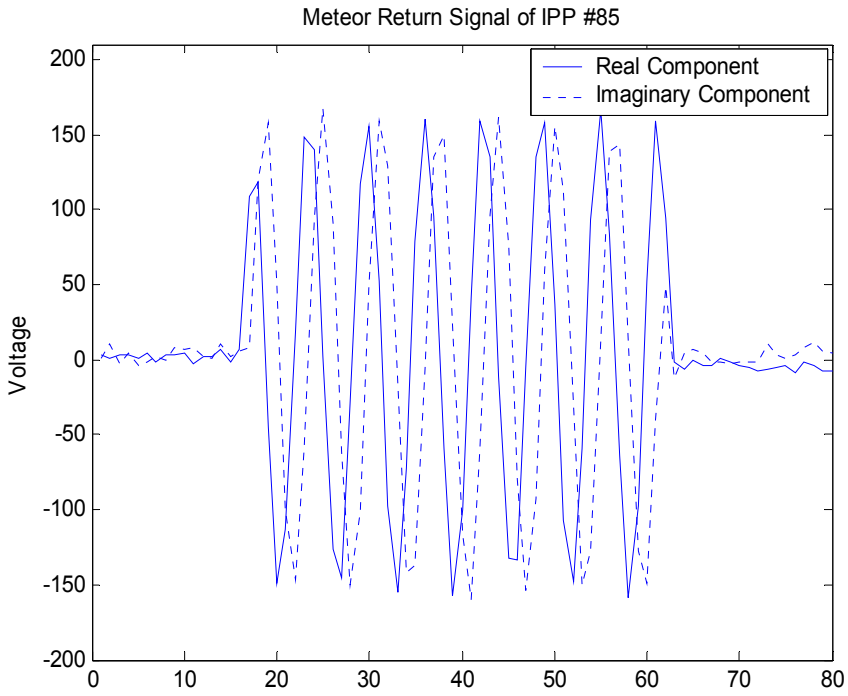

Fig. 2.2. Meteor return signal of IPP #85 of prototype meteor event.

2.2 Meteor Detection: Frequency Domain

2.2.1 Detection Process

The meteor detection technique is based on the Fast Fourier Transform (FFT) of a running time window which contains several IPPs, as shown in Fig. 2.3. When a meteor event is present in all IPPs of the window, there is a special Fourier series structure in the frequency spectrum because of the periodicity of the meteor return. We use window size 4 (4 consecutive IPPs in one window) to describe the detection mechanisms. Fig. 2.4 shows the magnitude of the frequency spectrum of the window which contains IPP #85 through IPP #88 of the prototype meteor event. The special pattern, which we term "Meteor Return Signature" (MRS), is clearly visible in Fig. 2.4(b). Note that the envelope of the MRS is a sinc function. Since each meteor event results in this spectral pattern, we construct a MRS correlator to detect the presence of the singal. Fig. 2.5 shows the block diagram of the meteor detector.

Using the FFT of several consecutive IPPs will enhance the detection, because all the energy of several meteor return signals adds coherently. For example, if the window size is 4 and the meteor return signals are all coherent, the magnitude of the MRS would be 4 times larger than the magnitude of the MRS of single IPP. In Arecibo radar data, there is a phase difference between the meteor return signals of two consecutive IPPs because the meteor is moving toward the radar. The phase difference is a function of the Doppler speed, thus the magnitudes of MRS will then be slightly less the coherent case, which is described in Section 2.2.2. Another source of detection degradation occurs when the meteor duration is less than the window size, i.e., additional noise is introduced at the input to the decision device

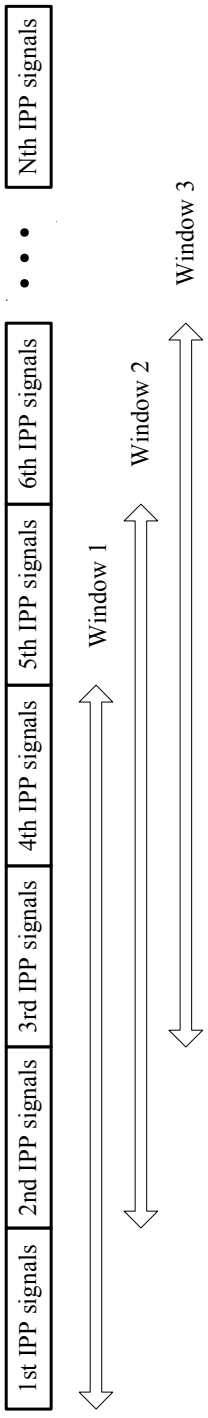

Figure 2.3: Sliding window analysis to detect the presence of meteor return signals. The window size is variable.

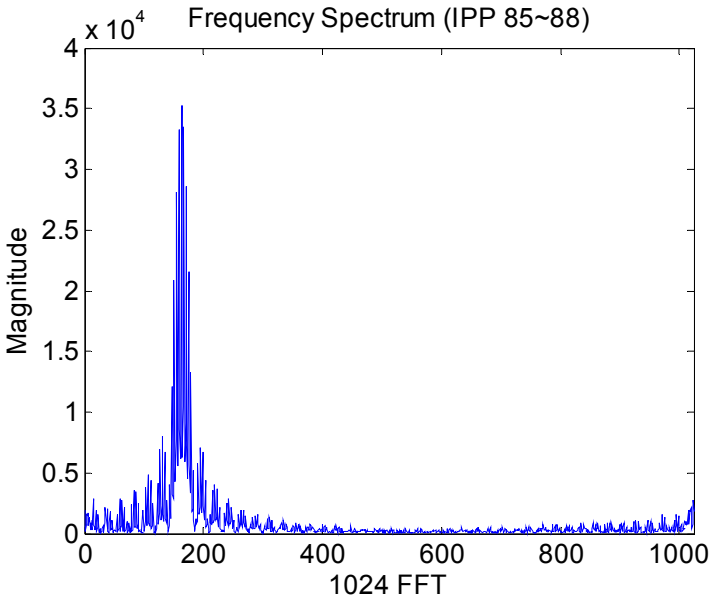

(a)

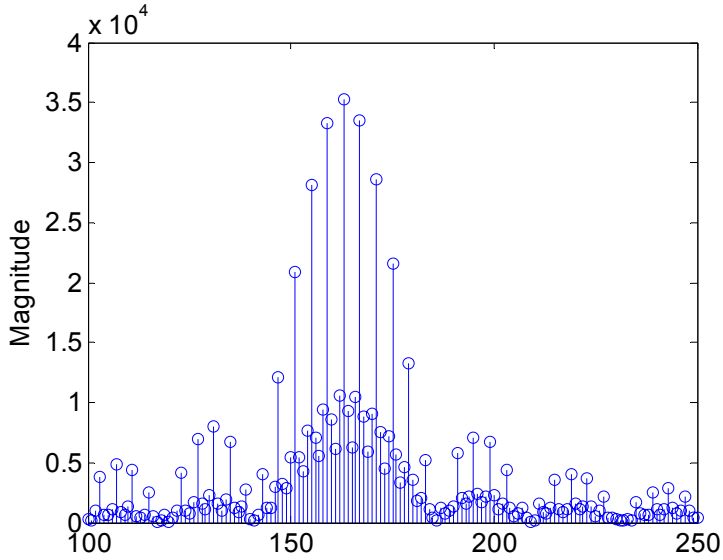

(b)

Figure 2.4: Example of the MRS (a) Frequency Spectrum of 4 consecutive IPPs (#85~#88). (b)Main lobe of part (a). We can see the Fourier Series pattern here.

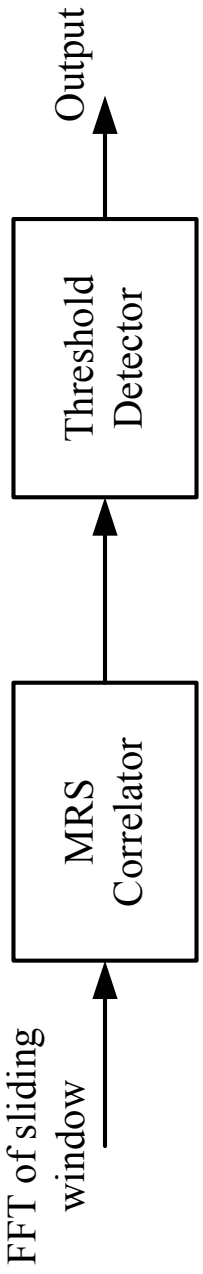

Figure 2.5: Block diagram of the meteor return signal detector.

For example, if the window size is four IPPs of which two IPPs contain meteor returns, the other two noise-only IPPs deteriorate the detection. To calculate the average missed detection probability for different window size, we assume the Doppler frequency, ω_D in (2.1); meteor return amplitude, A in (2.1); and meteor event durations to be random variables. We analyzed approximately 2000 meteor events recorded on February 24, 2001 to estimate the distributions of these parameters. Fig. 2.6 shows the distributions of the Doppler frequency and the meteor event durations. For different meteor duration, the amplitude distribution varies. Fig. 2.7 shows the distribution of the amplitude. Fig. 2.7(a) is the distribution of average amplitude for different meteor durations, which shows that higher SNR is associated with longer meteor events. Fig. 2.7(b) is one example of the probability mass function of the amplitude distribution for different event durations. In this case, the duration is 4-IPP. The detailed mathematical derivation for average missed detection probability vs. window size is described in Section 2.2.2. Fig. 2.8 shows the average missed detection probability vs. the window size. We can see that window size 2, 3, and 4 all outperform window size 1, which is the detection based on one IPP. The missed detection probabilities for these cases are very low.

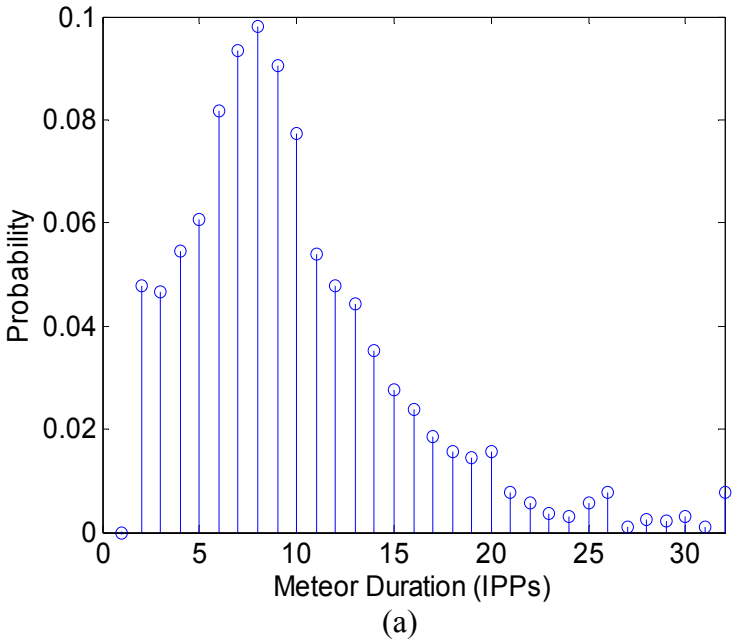

(a)

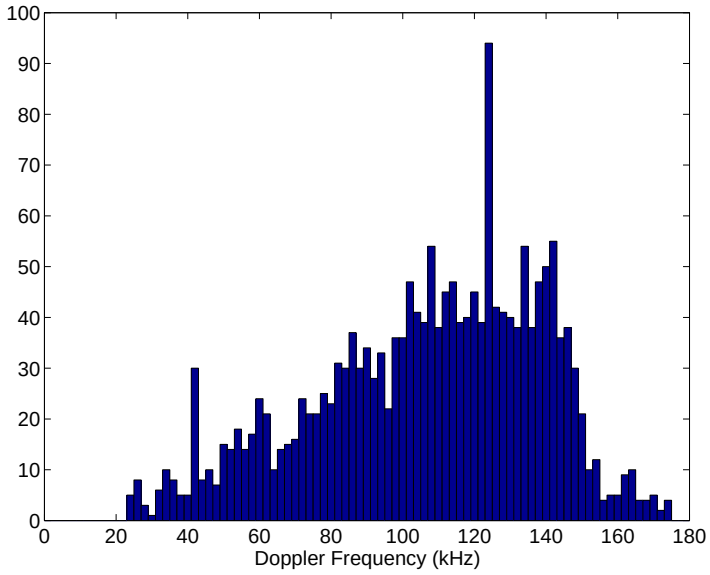

(b)

Figure 2.6: Distributions of the meteor event duration and Doppler frequency (a) The distribution of meteor event duration. (b) The histogram of the Doppler frequency. These distributions are from analyzing approximately 2000 events recorded on Feb. 24th 2001.

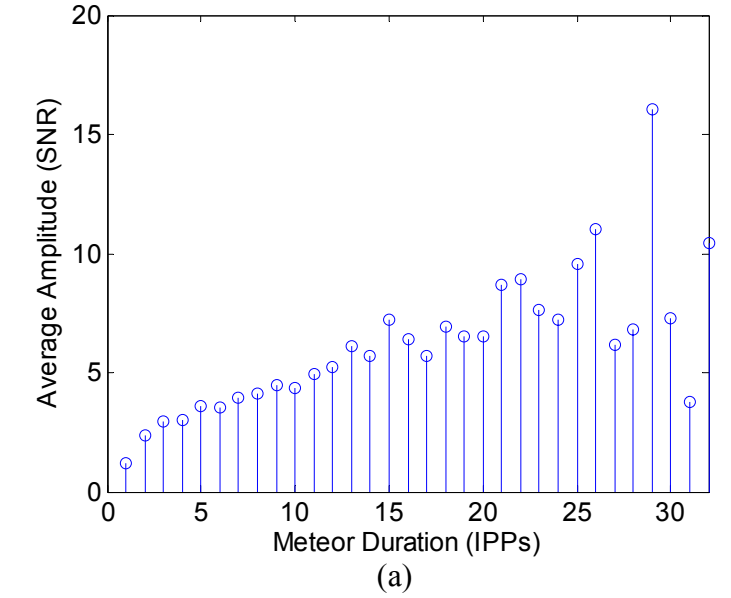

(a)

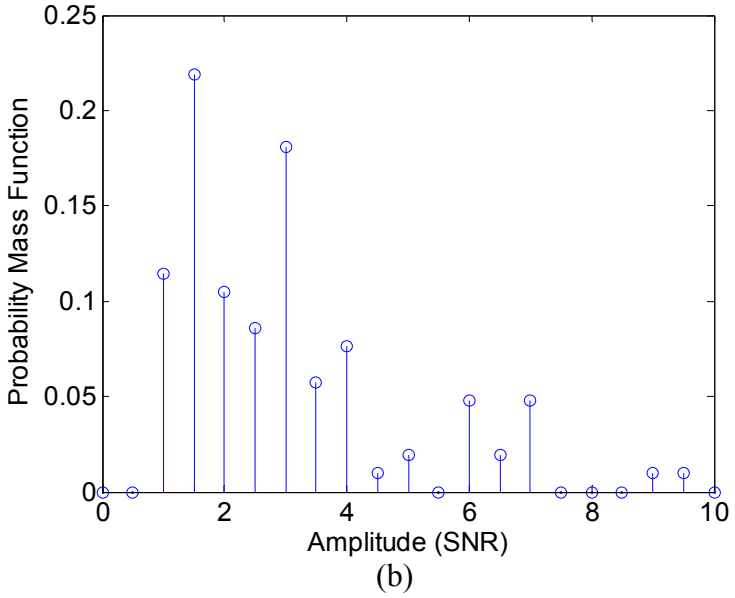

(b)

Figure 2.7: Distributions of the amplitudes (a) The average amplitude distribution as the function of meteor event duration. (b) Probability mass function of amplitude (in terms of SNR) for 4-IPP long meteor events. For the event with different duration, the distribution varies.

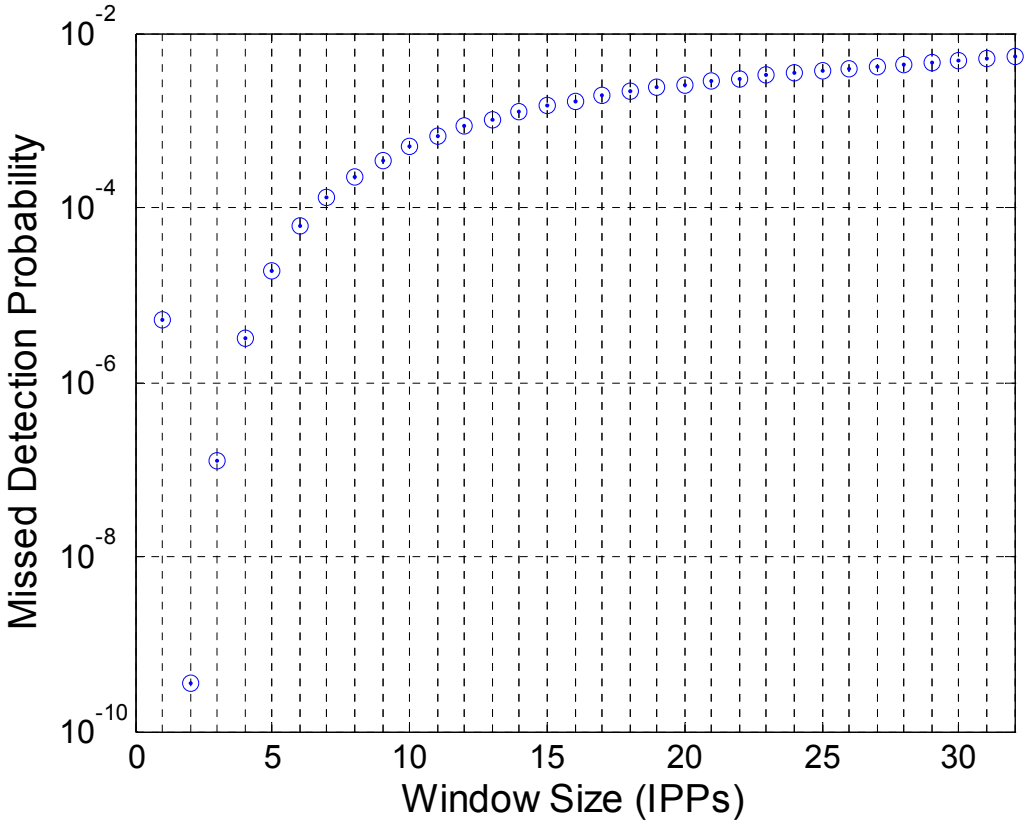

Figure 2.8: Average missed detection probability for different window size.

2.2.2 Mathematical Derivation of Missed Detection Probability for Different Window Size

For any given IPP with meteor return, the radar received signal is modeled by

$$r_{IPP}[n] = n_w[n] + A\exp\left\{j\left(\omega_D n + \phi\right)\right\}\Delta\left[n - l_M\right],\ n = 1, 2, ..., 250 \qquad (2.3)$$

where $n_w[n]$ is additive complex white noise, the second term in the right-hand-side of (2.3) corresponds to meteor return signal, $m[n]$, and we use $N_{IPP} = 250$ as 250 signal samples per IPP for the prototype meteor event. Let $n_{w,r}[n]$ and $n_{w,i}[n]$ be the real and imaginary parts of $n_w[n]$, respectively, and both are Gaussian distributed random variables with mean zero and variance σ^2. The location, l_M, of the meteor will not affect the magnitude of the frequency spectrum. So without loss of generality, we assume $l_M = 0$. The FFT of $r_{IPP}[n]$ is

$$R_{IPP}[k] = FFT\left\{r_{IPP}[n]\right\} = FFT\left\{n_w[n]\right\} + FFT\left\{m[n]\right\} = N_w[k] + M[k],\ k = 1, 2, ..., L \qquad (2.4)$$

where $N_w[k]$ and $M[k]$ are the FFT of $n_w[n]$ and $m[n]$, respectively, and L is the FFT length. Note that we can zero pad the original signal so L is a number larger or equal to 250. $M[k]$ is given by

$$M[k] = \sum_{t=1}^{45} Ae^{j(\omega_D t + \phi)} e^{-j\frac{2\pi}{L}kt} = A\frac{\sin\left[\frac{45}{2}\left(\frac{2\pi}{L}k - \omega_D\right)\right]}{\sin\left[\frac{1}{2}\left(\frac{2\pi}{L}k - \omega_D\right)\right]} e^{j\phi - j23\left(\frac{2\pi}{L}k - \omega_D\right)} \qquad (2.5)$$

$$\left|M[k]\right| = 45A\left|\frac{\operatorname{sinc}\left[\frac{45}{2}\left(\frac{2\pi}{L}k-\omega_D\right)\right]}{\operatorname{sinc}\left[\frac{1}{2}\left(\frac{2\pi}{L}k-\omega_D\right)\right]}\right| \tag{2.6}$$

With the presence of a meteor, the magnitudes of the frequency bins of $R_{IPP}[k]$ are independent Rice-distributed random variables [17]. Otherwise the magnitudes of the frequency bins of $R_{IPP}[k]$ are independently Rayleigh-distributed [17].

Given the observed statistics of meteor events, we now determine the appropriate window size to minimize the missed detection probability. Assume that we collect W (the window size) IPPs, and p out of W IPPs have meteor return signals, where p is a random variable. Under these conditions, the radar received signal in the window is

$$r_W[n] = n_w[n] + m_1[n] + ... + m_p[n],\ n = 1,2,...,250W \tag{2.7}$$

where the number of signal samples of $r_W[n]$ is $250W$, because each window contains 250 complex voltage samples; $m_i[n],\ i = 1,2,...,p$ are the meteor return signals. They are expressed as

$$\begin{aligned} m_1[n] &= A\exp\left\{j(\omega_D n+\phi)\right\}\Delta[n], \\ m_i[n] &= m_1[n-250(i-1)]\exp\left\{j(i-1)\theta\right\},\ i = 2,3,...,p \end{aligned} \tag{2.8}$$

where we assume the Doppler frequencies of all the meteor return signals in (2.8) from one event are identical, and $l_M = 0$. θ is the phase difference between two consecutive IPPs, which can be expressed as

$$\theta = \left(k_D \times \frac{D_{1\text{ msec}}}{2}\right) \bmod 2\pi \tag{2.9}$$

where "mod" is modulus operation, $D_{1\text{msec}}$ is the signal traveling distance in 1 mille second, which is 300 meters, and k_D is the wave number. We then have

$$k_D = \frac{2\pi}{\lambda} \tag{2.10}$$

$$\lambda = \frac{3\times 10^8}{(430 + f_D)\times 10^6} = \frac{300}{430 + f_D} \tag{2.11}$$

$$f_D = \frac{K}{L}\times 1\ MHz \tag{2.12}$$

where f_D is the Doppler frequency, λ is the wavelength of received radar pulse, and K is the position of the peak magnitude in the L-point FFT. Substituting (2.10), (2.11), and (2.12) into (2.9) yields

$$\theta = \left(430 + \frac{K}{L}\right)\pi \bmod 2\pi = \frac{\mathrm{K}}{\mathrm{L}}\pi \tag{2.13}$$

To simplify the analysis, we assume that the amplitude, A in (2.8), is constant for the whole event. The FFT of $r_W(n)$ is

$$\begin{aligned} R_W[k] &= N_W[k] + M_1[k] + \ldots + M_p[k] \\ &= N_W[k] + M_1[k]\left[1 + e^{-j\left(\frac{2\pi k}{L}-\omega_D\right)*250} e^{j\theta} + \ldots + e^{-j(p-1)*\left(\frac{2\pi k}{L}-\omega_D\right)*250} e^{j(p-1)\theta}\right] \end{aligned} \tag{2.14}$$

where the upper case quantities are the FFTs of the corresponding lower case quantities and, L is the FFT length.

Let $M_{p,W}[k] = M_1[k]F[k]$ where $M_1[k]$ is given by (2.5), and

$$F[k]=1+e^{-j\left(\frac{2\pi k}{L}-\omega_D\right)*250}e^{j\theta}+e^{-j2*\left(\frac{2\pi k}{L}-\omega_D\right)*250}e^{j2\theta}+\ldots+e^{-j(p-1)*\left(\frac{2\pi k}{L}-\omega_D\right)*250}e^{j(p-1)\theta}$$

$$=\frac{1-e^{-jp\left[\left(\frac{2\pi k}{L}-\omega_D\right)*250-\theta\right]}}{1-e^{-j\left[\left(\frac{2\pi k}{L}-\omega_D\right)*250-\theta\right]}}=e^{-j\frac{p-1}{2}\left[\left(\frac{2\pi k}{L}-\omega_D\right)*250-\theta\right]}\frac{\sin\left[\frac{p}{2}\left(\frac{2\pi k}{L}-\omega_D\right)*250-\frac{p}{2}\theta\right]}{\sin\left[\frac{1}{2}\left(\frac{2\pi k}{L}-\omega_D\right)*250-\frac{1}{2}\theta\right]} \quad (2.15)$$

$$\left|F[k]\right|=\left|\frac{\sin\left[\frac{p}{2}\left(\frac{2\pi k}{L}-\omega_D\right)*250-\frac{p}{2}\theta\right]}{\sin\left[\frac{1}{2}\left(\frac{2\pi k}{L}-\omega_D\right)*250-\frac{1}{2}\theta\right]}\right| \quad (2.16)$$

$$\left|M_{p,W}[k]\right|=45A\left|\frac{\operatorname{sinc}\left[\frac{45}{2}\left(\frac{2\pi}{L}k-\omega_D\right)\right]}{\operatorname{sinc}\left[\frac{1}{2}\left(\frac{2\pi}{L}k-\omega_D\right)\right]}\right|\left|\frac{\sin\left[\frac{p}{2}\left(\frac{2\pi}{L}k-\omega_D\right)*250-\frac{p}{2}\theta\right]}{\sin\left[\frac{1}{2}\left(\frac{2\pi}{L}k-\omega_D\right)*250-\frac{1}{2}\theta\right]}\right| \quad (2.17)$$

Now we have $R_W[k]=N_W[k]+M_{p,W}[k]$. Note that $\left|F[k]\right|\le p$. From equation (2.17), for a coherent meteor return signal, i.e. θ=0, $\left|M_{p,W}[k]\right|$ is a Fourier series and the magnitude of $\left|M_{p,W}[k]\right|$ is p times larger than $\left|M[k]\right|$. For the noncoherent case, i.e. $\theta\neq 0$, $\left|M_{p,W}[k]\right|$ is slightly less than $p\times\left|M[k]\right|$.

The magnitudes of $R_W(k)$, with the presence of meteor return signal, are Rice-distributed random variables with noncentrality parameter equal to $\left|M_{p,W}[k]\right|^2$. Otherwise, they are Rayleigh-distributed [17].

For the detector, we use the normalized magnitudes of main lobe of *M(k)*, adjusted according to the window size, as the impulse response. If the MRS is in the input spectrum, the correlator output will produce a peak. Let $R_W[k]$, $H[k]$, $Y[k]$ be the input, impulse response, and output of the MRS correlator, respectively. Then

$$Y[k] = \left| R_W[k] \right| * H[k] \tag{2.18}$$

where "$*$" denotes convolution. The magnitude of each frequency bin of *Y(k)* is the summation of nine independent Rice-distributed or Rayleigh-distributed random variables depending upon the presence of a meteor return signal. By the Central Limit Theorem (CLT) [11], we use a Gaussian random variable to approximate the magnitude distribution of *Y(k)* for either Rayleigh or Rice distributed case. The mean μ_S and the variance σ_S^2 of this Gaussian distribution can be expressed as

$$\mu_S = \sum_{i=-4}^{4} \mu_i H[iW] \tag{2.19}$$

$$\sigma_S^2 = \sum_{i=-4}^{4} \sigma_i^2 H^2[iW] \tag{2.20}$$

where μ_i and σ_i^2 are mean and variance of Rice (Rayleigh) distribution with (without) the presence of meteor return signal. We then use the Maximum Likelihood (ML) criterion to calculate the missed detection probability. For a 0 dB SNR meteor return signal, i.e., A=1 and σ^2=1/2 in equation (2.3), and Doppler speed 52km/sec with window size 4 (assuming event duration is longer than 4-IPP), the missed detection probability is approximately 0.15%. The average missed detection probability for different window sizes is expressed as

$$\begin{aligned} &\text{Prob}\left\{\text{Missed Detection} \middle| \text{Window Size}\right\} \\ &= \int \text{Prob}\left\{\text{Missed Detection} \middle| \begin{matrix}\text{Window Size, Doppler Frequency,} \\ \text{Amplitude, Meteor Duration}\end{matrix}\right\} \\ &\quad \times f\left(\begin{matrix}\text{Doppler Frequency,} \\ \text{Amplitude, Meteor Duration}\end{matrix}\right) df \end{aligned} \tag{2.21}$$

where $f(\bullet)$ is the joint probability density function. To simplify the analysis, we assume the Doppler frequency, amplitude, and meteor duration are mutually independent. We then use the distributions of meteor duration, amplitude, Doppler frequency (shown in Fig. 8 and 9), and equations (2.13), (2.14), (2.17), (2.18), (2.19), (2.20), and (2.21) to get the magnitude distribution of Doppler frequency and to calculate missed detection probability.

2.3 Meteor Detection: Time Domain

As in frequency domain, we can also detect a meteor event in time domain. We construct a filter bank containing 256 filters. The impulse response of each filter is

$$h_i[n] = A_i \exp\left\{-j\left(\omega_i n + \phi_i\right)\right\} \Delta[-n],\ i = 1,2,\ldots,256 \tag{2.22}$$

where A_i is the amplitude, ω_i is the center frequency corresponding to Doppler speed ranging from 0 km/sec to 175 km/sec, ϕ_i is the phase of each filter, and $\Delta[n]$ is the same as (2.2). Fig. 2.9 shows the block diagram of the filter bank.

The input of the filter bank is one IPP, expressed as (2.3), and the output of each filter, $y_i[n],\ i=1,2,\ldots,256$, is expressed as

$$y_i[n] = r_{IPP}[n] * h_i[n] = \sum_{m=-\infty}^{\infty} A e^{j(\omega_D m+\phi)} \Delta[m - l_M] \times A_i e^{-j\left[\omega_i (n-m)+\phi_i\right]} \Delta[m-n] \tag{2.23}$$

Notice that when $n = l_M$ and $\omega_i = \omega_D$, we will have the maximum output. The estimated Doppler frequency is then expressed as

$$\hat{\omega}_D = \arg \max_{\omega_i} \left| y_i[n] \right|,\ i = 1,2,\ldots,256 \tag{2.24}$$

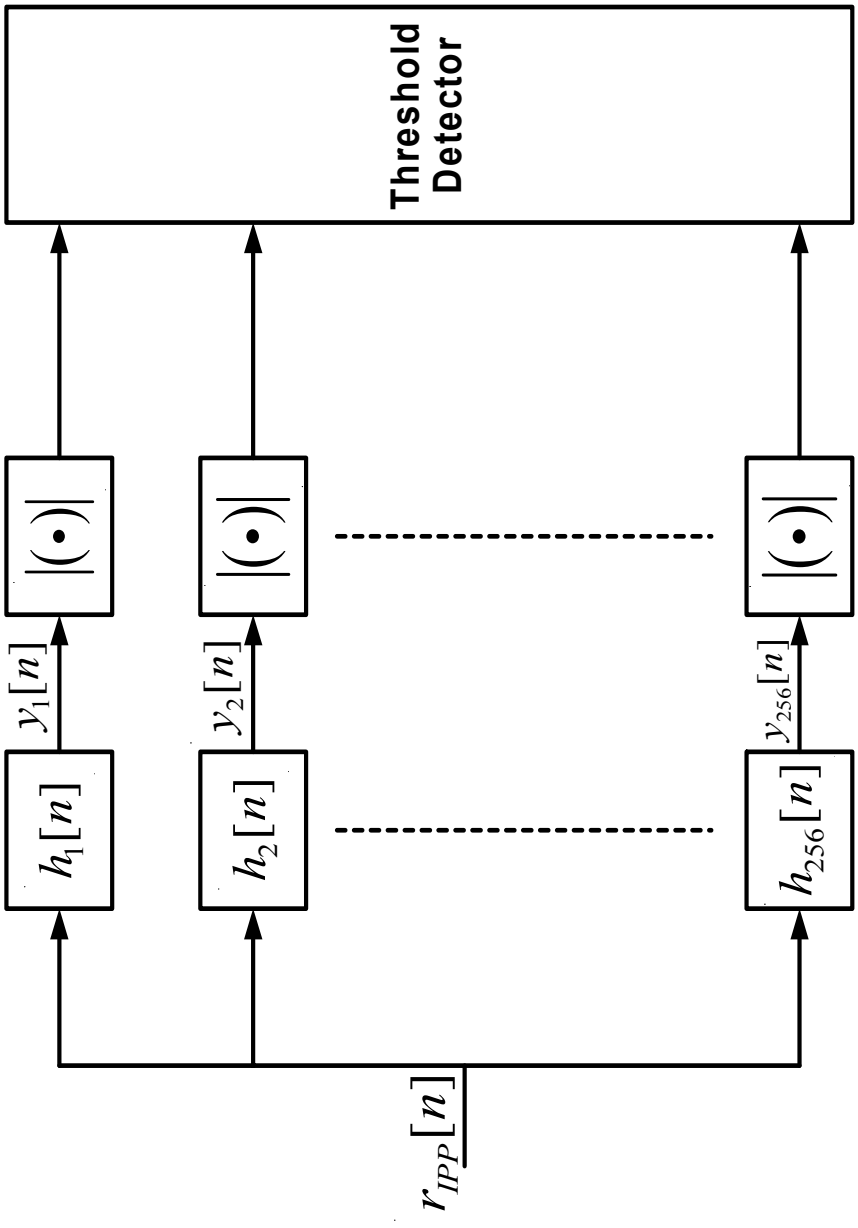

Figure 2.9: The block diagram of the filter bank.

The location of the meteor return signal is expressed as

$$l_M = \arg \max_n \left| y_i[n] \right|_{\omega_i = \hat{\omega}_D} \tag{2.25}$$

The resolution of this filter bank is approximately 0.68 km/sec. In theory, we can construct a filterbank which matches the intrinsic resolution of Doppler velocity defined by the inverse of the pulse width.

2.4 Short Time Fourier Transform Analysis

With the prior knowledge of the 45-μs meteor return signal (45 signal samples in one received IPP), we develop the short time Fourier transform (STFT) method which improves the performance of the frequency domain meteor detection process in terms of reducing the noise level. Instead of using the whole IPP signals for the running window FFT, we use windowed signal frame, which contains 45 signal samples from each IPP, to do the running window FFT. For example, windowed signal frame #1 contains the 1st~45th signal samples from each IPP; windowed signal frame #2 contains 2nd~46th signal samples from each IPP, and so on so forth. Assume each IPP has N_{IPP} signal samples, this method has $N_{IPP} - N_{TP} + 1$ windowed signal frames, where N_{TP} is the length of transmitted pulse. For the prototype meteor event shown in Fig. 2.1, N_{IPP} and N_{TP} are equal to 250 and 45, respectively. The windowed signal frame is expressed as

$$WSF_{fn} = \begin{bmatrix} r_{IPP\#1}[m], ..., r_{IPP\#1}[m+44], r_{IPP\#2}[m], ..., r_{IPP\#2}[m+44], ..., \\ r_{IPP\#W}[m], ..., r_{IPP\#W}[m+44] \end{bmatrix} \tag{2.26}$$

where *fn* is the frame number, $r_{IPP\#n}[\bullet]$ is the signal of *n*th IPP in the running window. The short time Fourier transform (STFT) is the FFT of the windowed signal frame. When we get the correct 45 meteor signal samples, we have a maximum MRS in the frequency spectrum. This method eliminates those samples which are not meteor return signal. In other words, it reduces the noise level which makes the meteor detection easier.

Fig. 2.10 shows the examples of the STFT for different windowed signal frames. We use #69~#70 IPPs (window size 2) of the prototype meteor event shown in Fig. 2.1 for the demonstration. Fig. 2.10(a) shows the frequency spectrum of the running window using the whole IPP signals. We can see a weak MRS in the plot. Fig. 2.10(b) shows the STFT of the windowed signal frame #1, which contains incoherent scatter signals and the noise. Fig. 2.10(c) shows the STFT of the windowed signal frame #90, which contains about half of the meteor return signals (23 signal samples). We can see the MRS rises up from the noise level. Fig. 2.10(d) shows the STFT of the windowed signal frame #112, which contains all the meteor return signals. The MRS is clearly visible here. We can see the noise level is much lower in Fig. 2.10(d) compare to Fig. 2.10(a), which makes the meteor easily be detected.

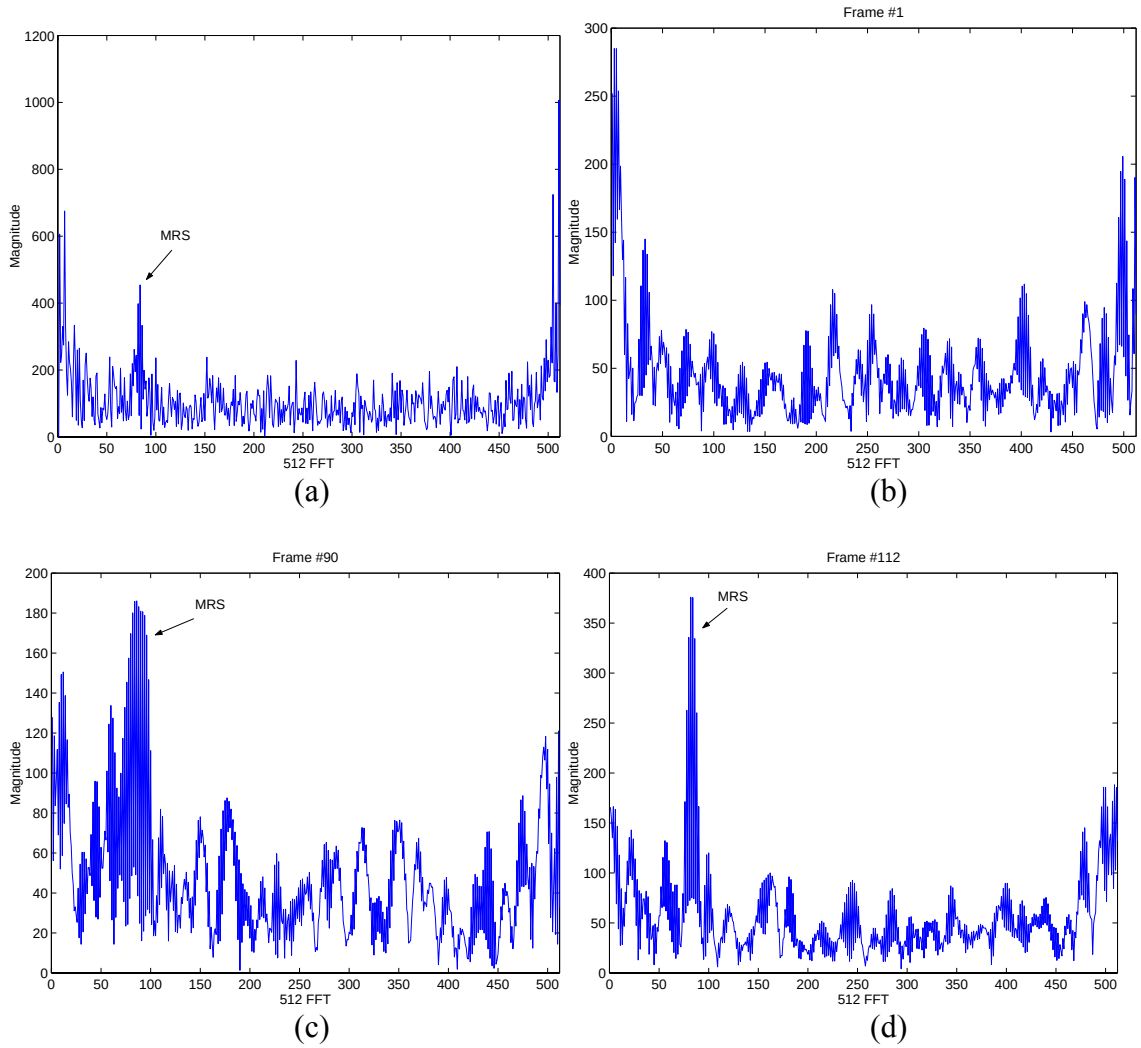

Figure 2.10: STFT analysis (a) The FFT of the running window contains IPP #69~#70 of the prototype meteor event. (b) The STFT of the windowed signal frame #1, which contains incoherent scatter signals and the noise. (c) The STFT of the windowed signal frame #90, which contains about half of the meteor return signals. (d) The STFT of the windowed signal frame #112, which contains all the meteor return signals. The MRS is clearly visible here.

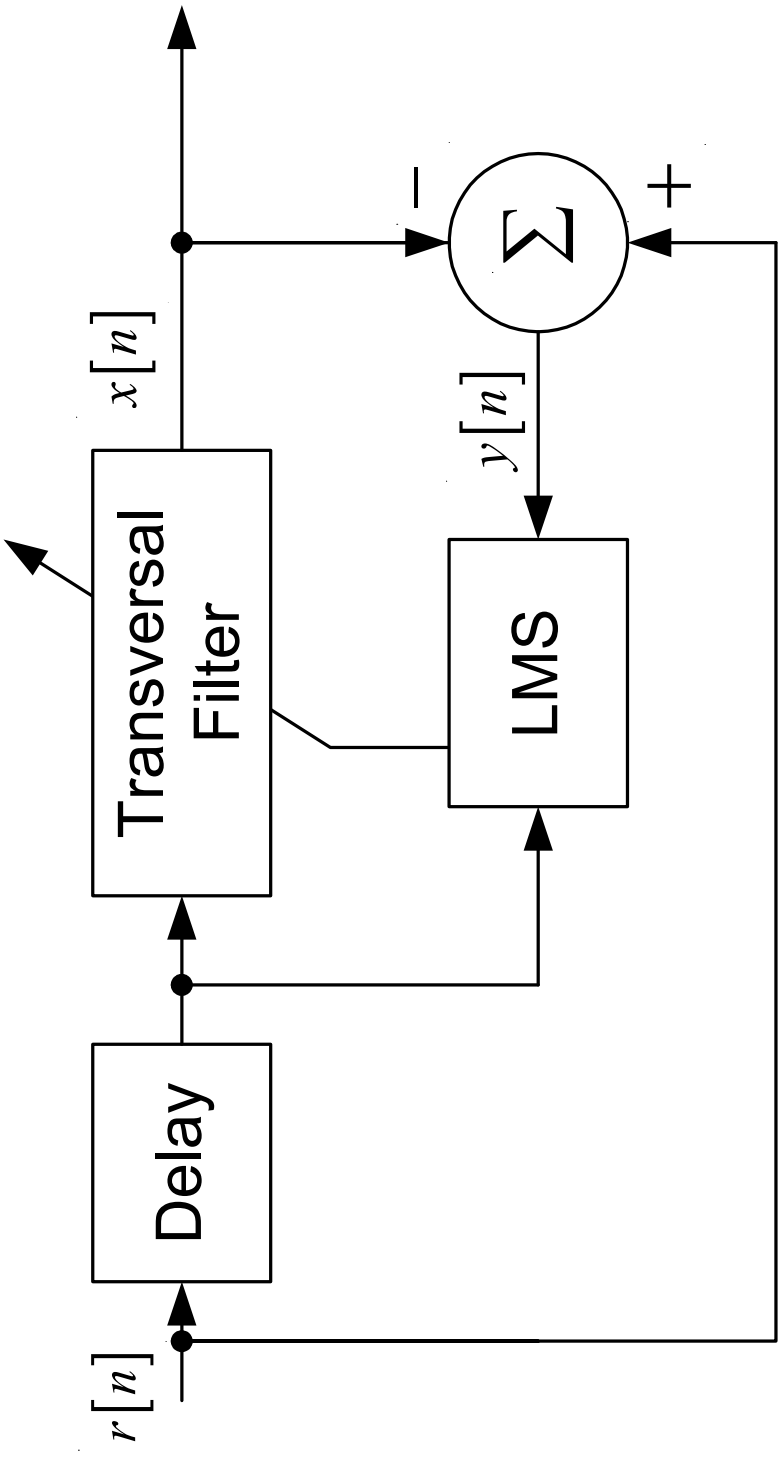

Figure 2.11: Block diagram of the LMS adaptive filter.

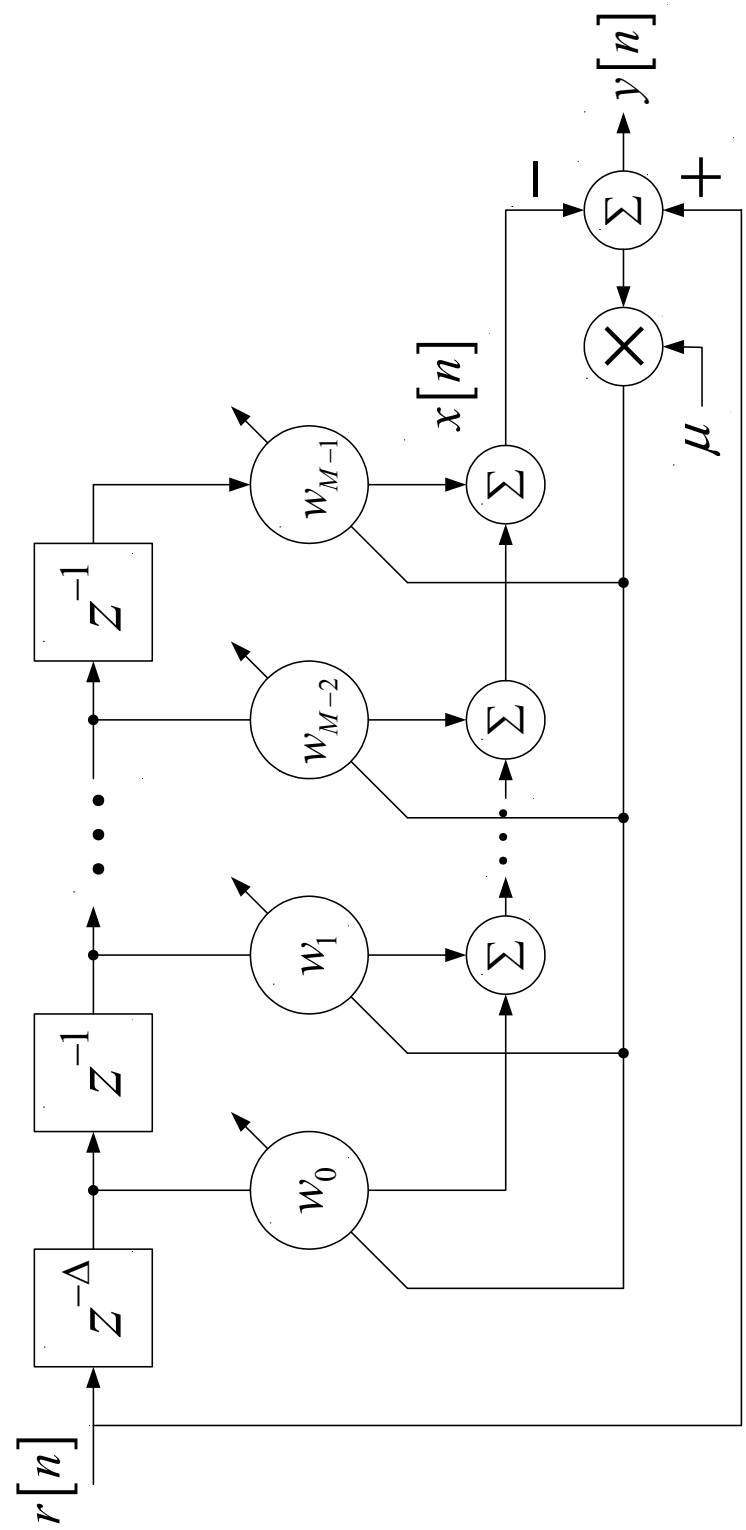

Figure 2.12: System structure of the LMS adaptive filter.

2.5 Adaptive Filter Technique for the Meteor Observation Data

To separate the incoherent scatter signals from other signals (meteor, white noise) we apply a Least-Mean-Square (LMS) adaptive filter [19] to the received radar signals. Fig. 2.11 and Fig. 2.12 are the block diagram and the system structure of the adaptive filter. The signals, r[n], x[n], and y[n] in the diagram are the received, estimated, and desired signals, respectively. The $z^{-\Delta}$, $w_{\#}$, and μ in the diagram are the delay (measured in units of the sampling period), filter coefficients, and the step size, respectively. The LMS adaptation algorithm is describes as the following [19]:

$$x[n] = \hat{\mathbf{w}}^{H}[n]\hat{\mathbf{r}}[n-\Delta] \tag{2.27}$$

$$y[n] = r[n] - x[n] \tag{2.28}$$

$$\hat{\mathbf{w}}[n+1] = \hat{\mathbf{w}}[n] + \mu\hat{\mathbf{r}}[n-\Delta]y^{*}[n] \tag{2.29}$$

where $\hat{\mathbf{r}}[n-\Delta] = \left[r[n-\Delta], r[n-\Delta-1], ..., r[n-\Delta-M+1]\right]^{T}$ is the input vector, μ is the step size, $\hat{\mathbf{w}}[n] = \left[w_0, w_1, ..., w_{M-1}\right]^{T}$ is the weight (filter coefficient) vector, the superscript H denotes Hermitian transposition (transposition combined with complex conjugation), and the superscript $*$ denotes the complex conjugation. The weights are recursively adjusted by the LMS algorithm to minimize the mean-square error between input and output signals. The step size μ determines how fast the filter converges to the minimum error. (Please refer to [19] for the details of the LMS adaptive filter.) This system is also called adaptive line enhancer (ALE) [19] which is used to detect a sinusoidal signal buried in a noise background. The input and output of the transversal filter are the delayed version of input signal and the estimated input signal, respectively.

When the input signals only consist of the white noise and incoherent scatter signals, which is usually the case since the meteor signal is rare, the transversal filter is a low pass filter (the frequency response is adaptively adjusted according to the input signal) which separates the incoherent scatter signal (x[n]) and the white noise(y[n]). In practice we first use the data with incoherent scatter and white noise signals to train this system. After it converges, we apply the meteor observation data as the input to the system and adjust the step size so that the filter responses slowly when there are meteor return signals. The meteor signals will then appear in y[n] (without incoherent scatter signals) as the result.

2.6 Experimental Results

In this section, we apply the algorithms described in section 2.2 ~ 2.5 to detect the meteor return signals of the radar data from Arecibo Observatory. We choose two relatively low SNR meteor return events shown in Fig. 2.13 and the one shown in Fig. 2.1 as the examples.

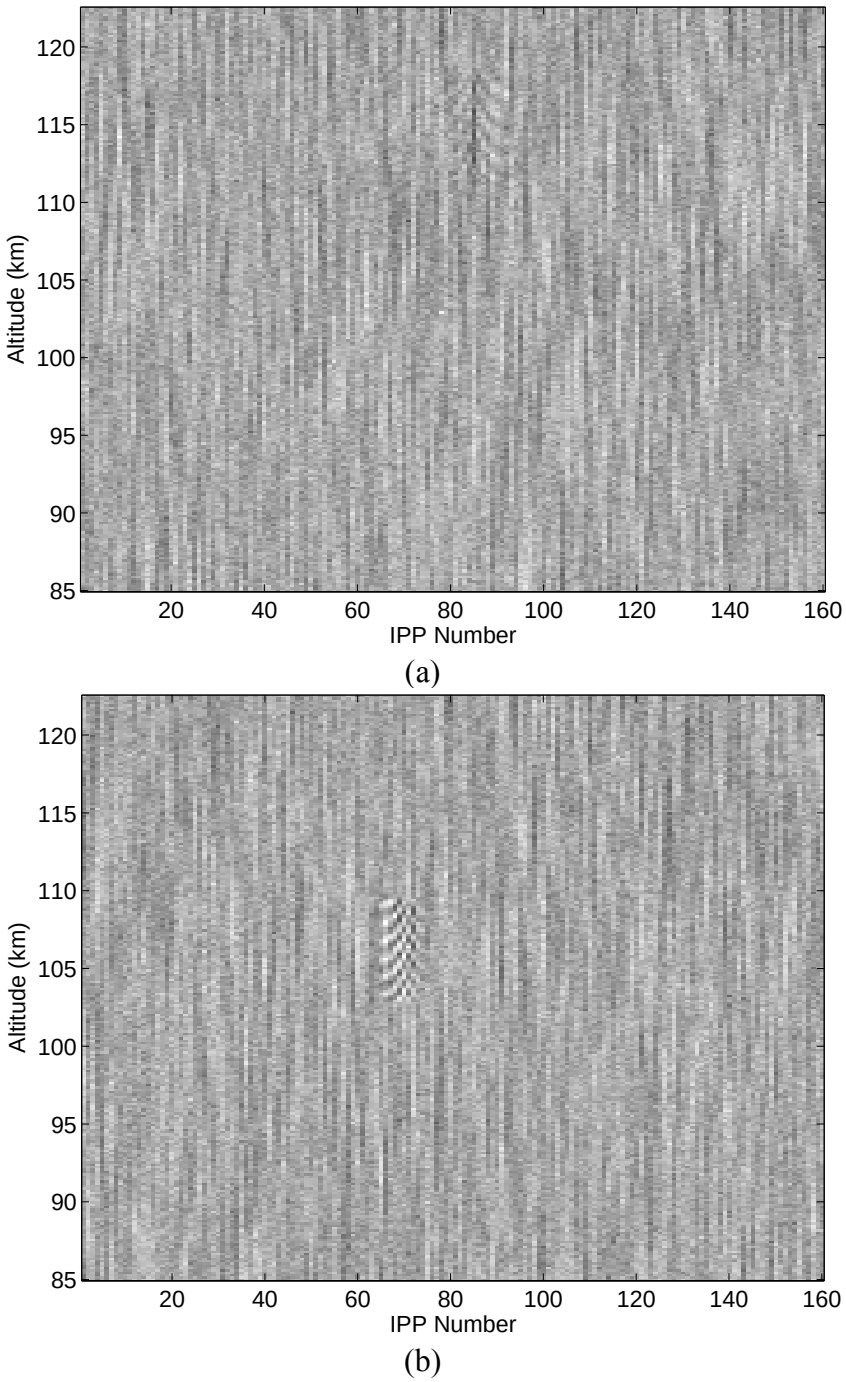

Figure 2.13: Real part of complex voltages of two different meteor events. (a) This event was recorded at 07:40:13.000 AST 24 Feb 2001. (b) This event was recorded at 07:40:18.192 AST 24 Feb 2001.

2.6.1 MRS Detection

We first apply the sliding window FFT to detect the MRS of the received signals. We choose the window size 2 which yields the minimum missed detection probability as shown in Fig. 2.8. Fig. 2.13 shows several examples of the frequency spectrum of sliding window and the results of the MRS correlator. The highest estimated SNR for the examples shown in Fig. 2.13(b) is approximately 30 dB, and the lowest SNR shown in Fig. 2.13(f) is approximately -10 dB. The low frequency part of the spectrum is due to elemental incoherent scatter [5]. The incoherent scatter can be separated from the meteor return signal because of its near orthogonality[1] with the meteor return signal in the frequency domain. It is obvious that the MRS correlator raises the peak higher above the noise level compared to the original frequency spectrum, which increases the probability of detection. Notice that for the event of IPP #127~128 in Fig. 2.13(b), it is very difficult to visually identify the meteor return signal.

2.6.2 Filterbank Detection

Fig. 2.15 shows the results of the filter bank for different meteor return signals. For high SNR meteor return signal, shown in Fig. 2.15(a), the output of the filter bank, shown in Fig. 2.15(b), is approximately a perfect triangle pattern. For low SNR cases, shown in Fig. 2.15 (c) and (e), the triangle patterns are noisy. Notice that the position of the peak of this triangle pattern corresponds to the estimated Doppler velocity and the altitude of the meteor. For example, the estimated Doppler velocity and the altitude of

[1] The frequency spectrums of the meteor and elemental incoherent scatter are both sinc functions. The side lobes of two different signals interact with each other but the effect is mild. We use "near orthogonality" to address this effect.

Fig. 2.15(b) are 55.3 km/sec and 100.6 km, respectively. We use this result to reconstruct the signal that matches the original one, as shown in Fig. 2.15(a), perfectly.

We then use a computer program which combines MRS and filter bank methods to automatically detect meteor events and determine the Doppler frequency and altitude of each event. We use the data recorded on February 24 2001. Fig. 2.16 shows the experimental result. We detect approximately 2000 events. The comparison of this result with the visually detecting result[2] shows that our algorithm can detect more meteor events.

2.6.3 Short Time Fourier Analysis

Fig. 2.17 shows some results of the running window FFT using the whole IPP and the results using STFT analysis for comparison. The left hand side plots are the results of the running window FFT using the whole IPP; the right hand side plots are the STFT analysis results which yield the maximum peak. Fig. 2.17(b) is the STFT of the signal sample number 183~227 from two IPPs of the meteor event shown in Fig. 2.13(a), which is the best estimation of the meteor event location. Fig. 2.17(d) is the STFT of the signal sample number 129~173 of the meteor event shown in Fig. 2.13(b), which is also the estimated meteor event location. We can see that the noise level is lower and the MRS shows up more clearly in the STFT analysis results, which makes the meteor detection easier. The drawback of this technique is we need much more computing power compared to the running window FFT using the whole IPP.

[2] The authors of previous works [4, 7] visually detect and analyze the raw data. For the very weak meteor events, as shown in Fig. 2.10(b) IPP #127~#128, it would be easily missed.

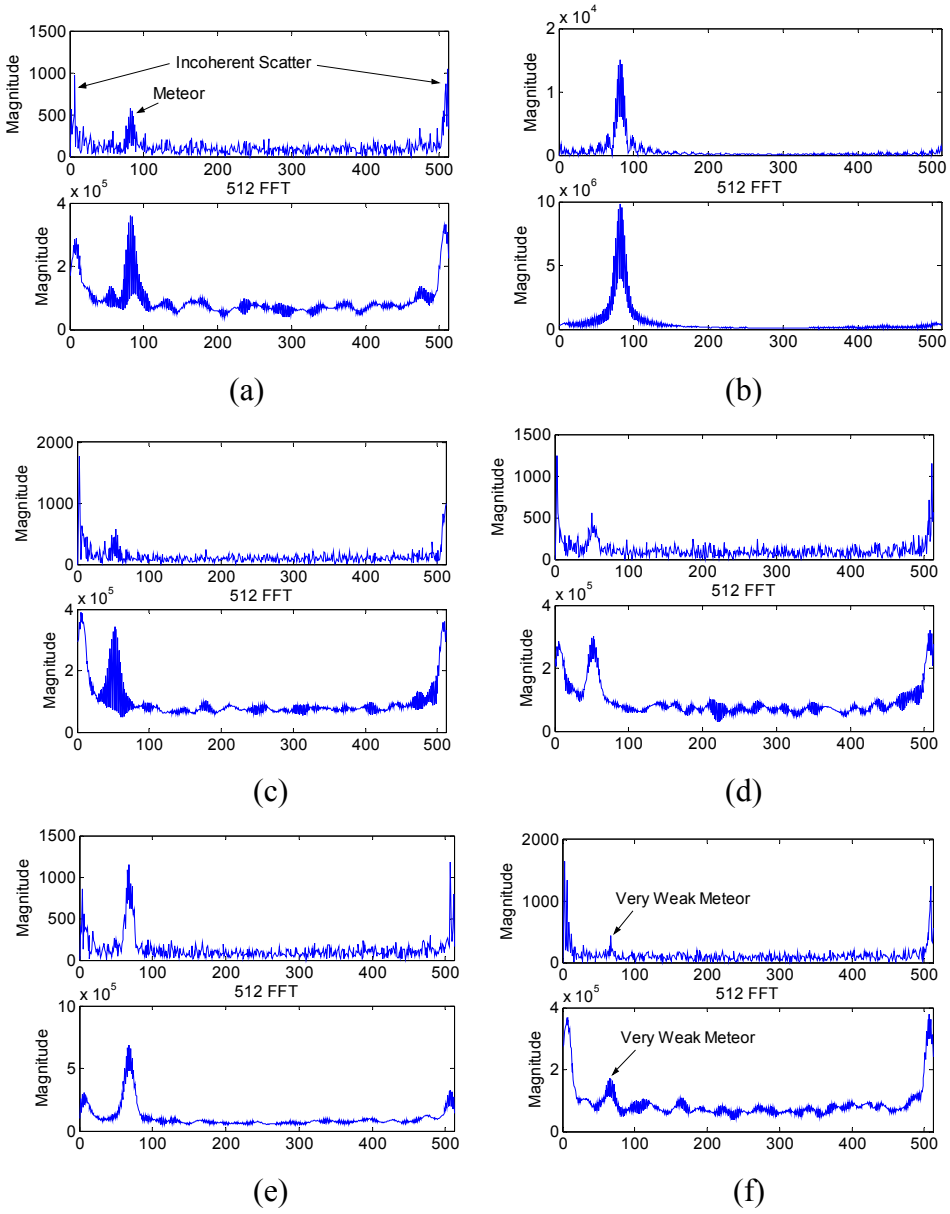

Figure 2.14: Examples of the MRS detector. These plots are the magnitude of frequency spectrum of different window from the three different meteor event examples (upper plot) and the results of the MRS correlator (lower plot). (a) IPP #70~71 of the meteor event shown in Fig. 2.1. (b) IPP #85~86 of the meteor event shown in Fig. 2.1. (c) IPP #85~86 of the meteor event shown in Fig. 2.13(a). (d) IPP #87~88 of the meteor event shown in Fig. 2.13(a). (e) IPP #68~69 of the meteor event shown in Fig. 2.13(b). (f) IPP#127~128 of the meteor event shown in Fig. 2.13(b).

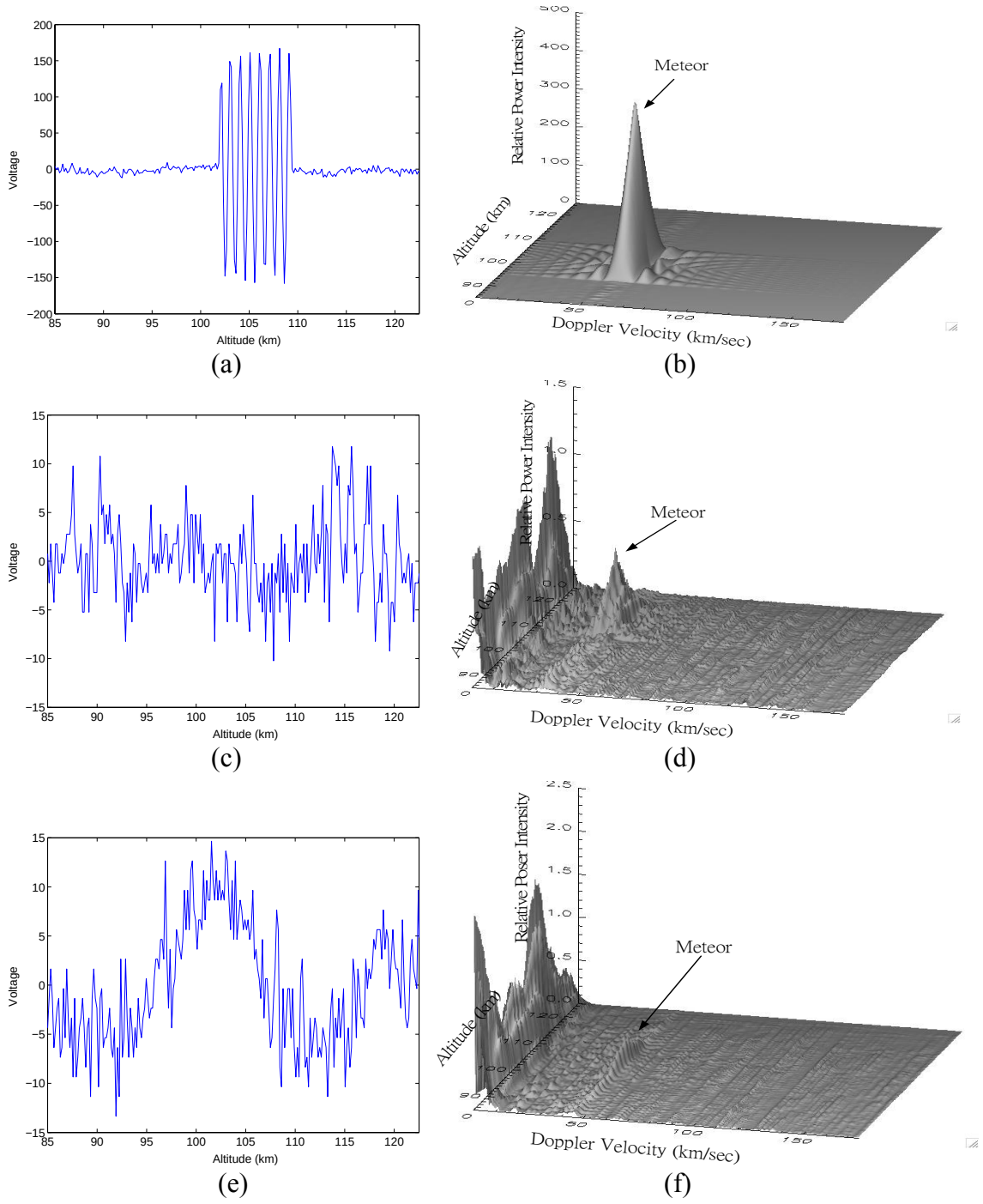

Figure 2.15: Examples of the meteor detection using the filter bank. These plots are the real part of the complex voltage and the results of the filter bank. (a) and (b) are IPP #85 of the event shown in Fig. 2.1. (c) and (d) are IPP #87 of the event shown in Fig. 2.13(a). (e) and (f) are IPP #128 of the event shown in Fig. 2.13(b).

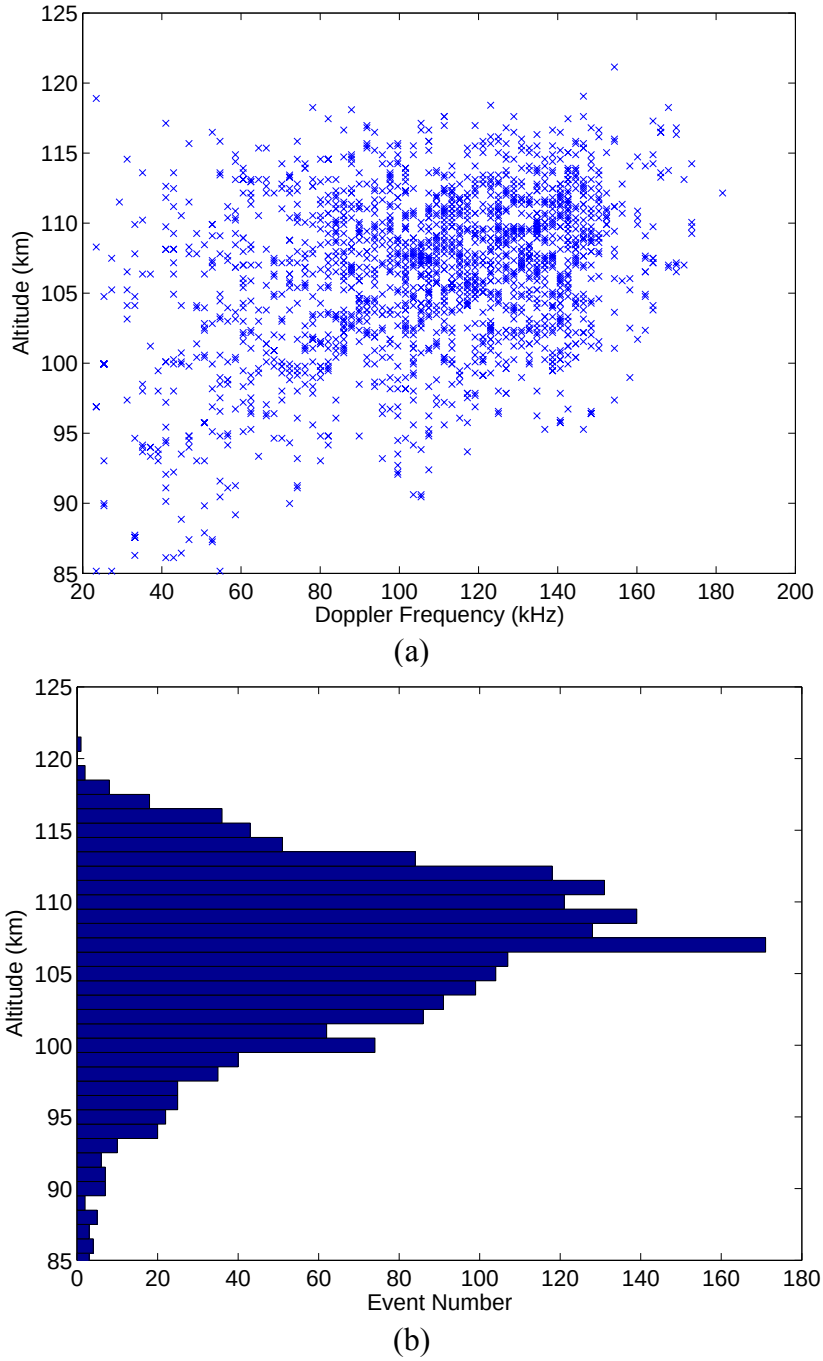

Figure 2.16: Results of automated detection process (a) The scatter plot of Doppler frequency vs. altitude for the meteor events. (b) The histogram of the distribution of the altitude. The histogram of the Doppler frequency is shown in Fig. 2.6 (b).

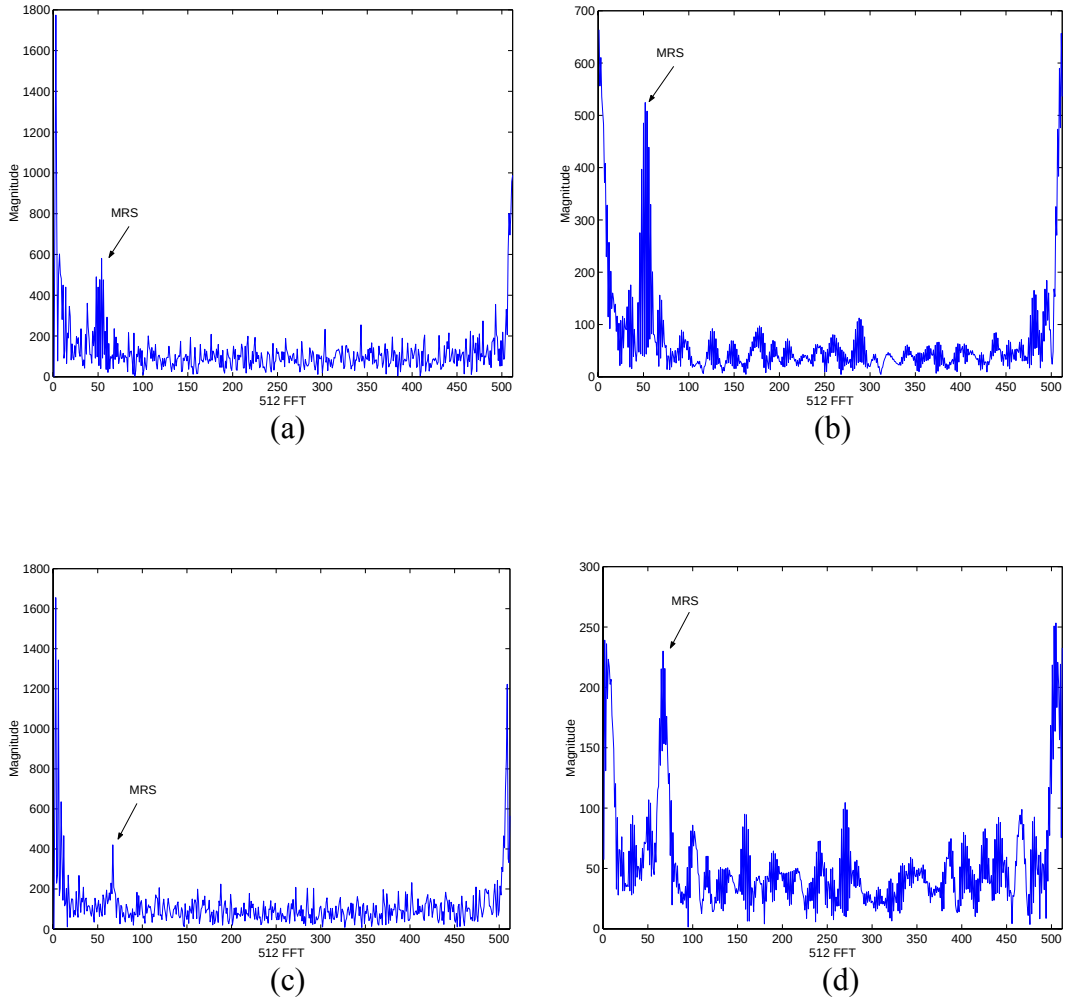

Figure 2.17: Comparison of the running window FFT using the whole IPP and the STFT analysis. The window size is 2. The left hand side plots are the results of the running window FFT using the whole IPP. The right hand side plots are the STFT analysis results which yield the maximum peak. (a) and (b) are IPP #85~#86 from the meteor event shown in Fig. 2.13(a). (c) and (d) are IPP #127~#128 from the meteor event shown in Fig. 2.13(b).

2.6.4 Adaptive Filter

We experimentally choose the length of the weight vector to be 8 and the time delay Δ to be 1. In other words we use $r[n-1],...,r[n-8]$ to estimate $r[n]$. Fig. 2.18 shows the results of applying the adaptive filter to the prototype meteor event shown in Fig. 2.1 and the corresponding frequency spectrums. Fig. 2.18 (a) and (b) are the real part of the complex voltages of IPP #150 and its frequency spectrum, respectively. Fig. 2.18 (c) and (e) are the $x[n]$ and $y[n]$ shown in Fig. 2.12. Fig. 2.18 (d) and (f) are the frequency spectrums of Fig. 2.18 (c) and (e), respectively. We can see that the adaptive filter almost perfectly estimates the incoherent scatter. It essentially is a low pass filter in this case. Fig. 2.19 shows the frequency response of the adaptive filter. Note that the frequency response adaptively changes depending on the input signal, but it is always a low pass filter.

Fig. 2.20 shows the results of applying the adaptive filter to the meteor event shown in Fig. 2.13(b). Fig. 2.20 (a) and (b) are the real part of the complex voltages of IPP #71 and its frequency spectrum. We can clearly see the incoherent scatter signal (low Doppler frequency) both in time and frequency domain. Fig. 2.20 (c) and (d) are the output of the adaptive filter ($y[n]$ in Fig. 2.12) and its frequency spectrum. We can see that the incoherent scatter signal is removed by the filter.

Fig. 2.21 shows the results of applying the adaptive filter to the meteor event shown in Fig. 2.13(a). Fig. 2.21 (a) and (b) are the real part of the complex voltages of IPP #87 and its frequency spectrum. Fig. 2.21 (c) and (d) are the output of the adaptive filter and its frequency spectrum. Again, we can see that the incoherent scatter signal is

removed by the filter. Note that the adaptive filter also slightly removes some energy of higher Doppler frequency signals, which causes slightly distortion of the meteor return signal.

2.6.5 Combination of Techniques

In this section we try to combine different techniques described in Section 2.2~2.5. We first combine the adaptive filter and the MRS correlator. Fig. 2.22(a) shows the flow chart of the experiment. We first use the adaptive filter to remove the incoherent scatter signal and then use the MRS correlator to detect the presence of a meteor event. For the MRS correlator we use window size 2 to do the analysis. Fig. 2.23 shows the results of running window FFT after applying the adaptive filter and the output of the MRS correlator. Fig. 2.23 (a) and (b) show the frequency spectrum (incoherent scatter signal removed) of the running window containing IPP #87~#88 of the meteor event shown in Fig. 2.13(a) and the result of the MRS correlator. Fig. 2.23 (c) and (d) show the frequency spectrum (incoherent scatter signal removed) of the running window containing IPP #127~#128 of the meteor event shown in Fig. 2.13(b) and the result of the MRS correlator. We can see that the incoherent scatter signals are removed and the correlator raises the MRS higher above the noise level.

Now we combine the adaptive filter, STFT analysis and the MRS correlator. We use the adaptive filter to remove the incoherent scatter signal first. Then we do the STFT analysis and use the MRS correlator to detect the meteor. Fig. 2.24 shows some experimental results. Fig. 2.24 (a) shows the STFT analysis result of the signal samples #183~#227 from IPP #87 and #88 of the meteor event shown in Fig. 2.13 (a) after

applying the adaptive filter. Compared to Fig. 2.17(b), which is the STFT analysis result without applying the adaptive filter, we can see the incoherent scatter signal is removed. Fig. 2.24 (b) shows the MRS correlator result of Fig. 2.24 (a). Fig. 2.24 (c) shows the STFT analysis result of the signal samples #129~#173 from IPP #127 and #128 of the meteor event shown in Fig. 2.13 (b) after applying the adaptive filter. Again we can see the incoherent scatter signal is removed. Fig. 2.24 (d) shows the MRS correlator result of Fig. 2.24 (c). Comparing Fig. 2.23 and Fig. 2.24 we can see the STFT analysis reduces the noise level and the correlator raises the MRS higher above the noise level, which make the detection of the meteor event easier.

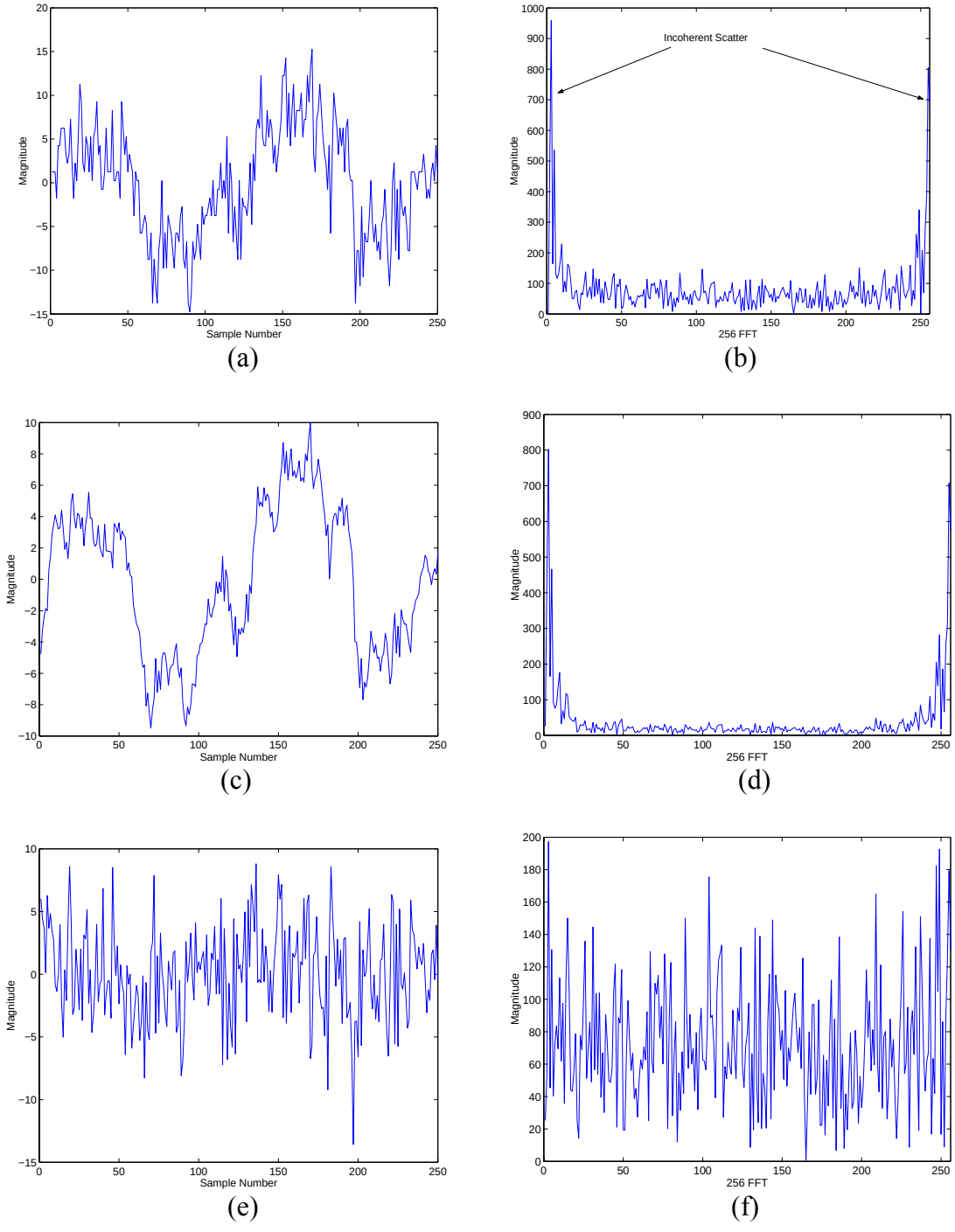

Figure 2.18: Results of the adaptive filter (a) Real part of the complex voltages of IPP #150 of the prototype meteor event. (b) Frequency spectrum of part (a). (c) The estimation of the adaptive filter, *x[n]* in Fig. 2.12. (d) Frequency spectrum of part (c). (d) The difference between the estimation and the real signal, *y[n]* is Fig. 2.12. (e) Frequency spectrum of part (d)

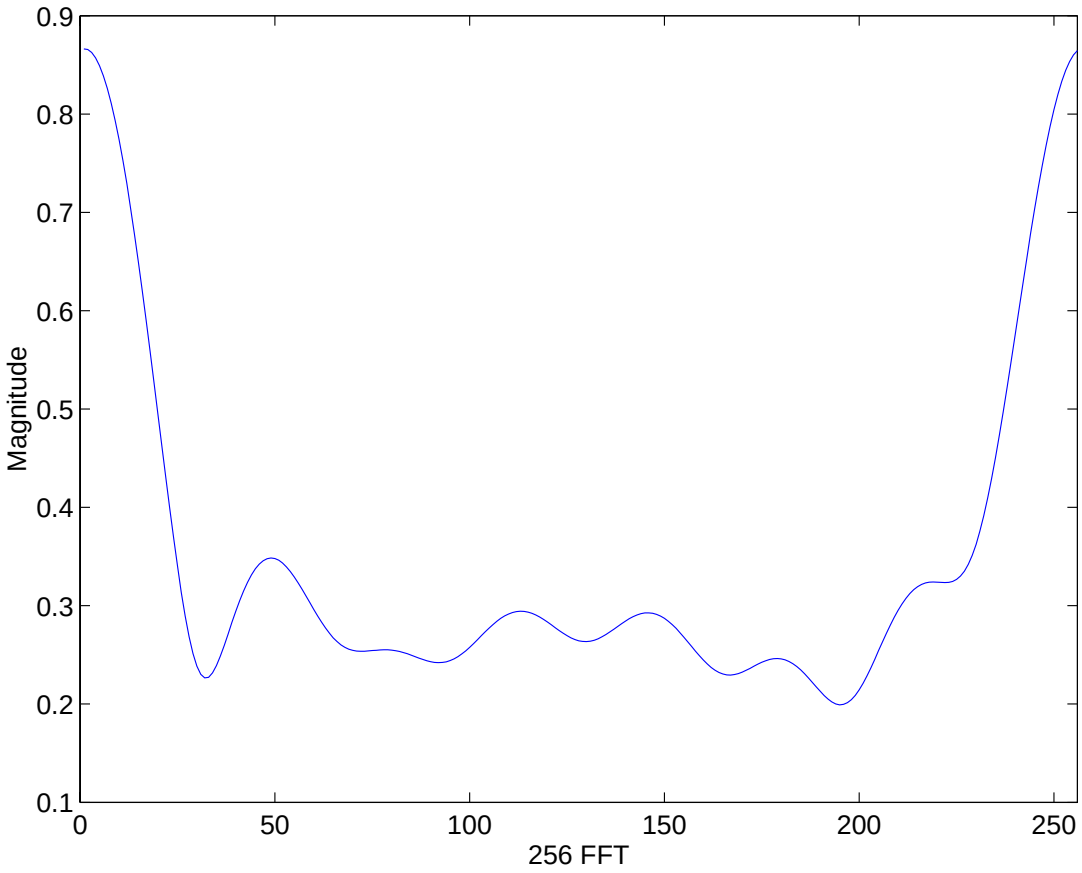

Figure2.19: Frequency response of the adaptive filter.

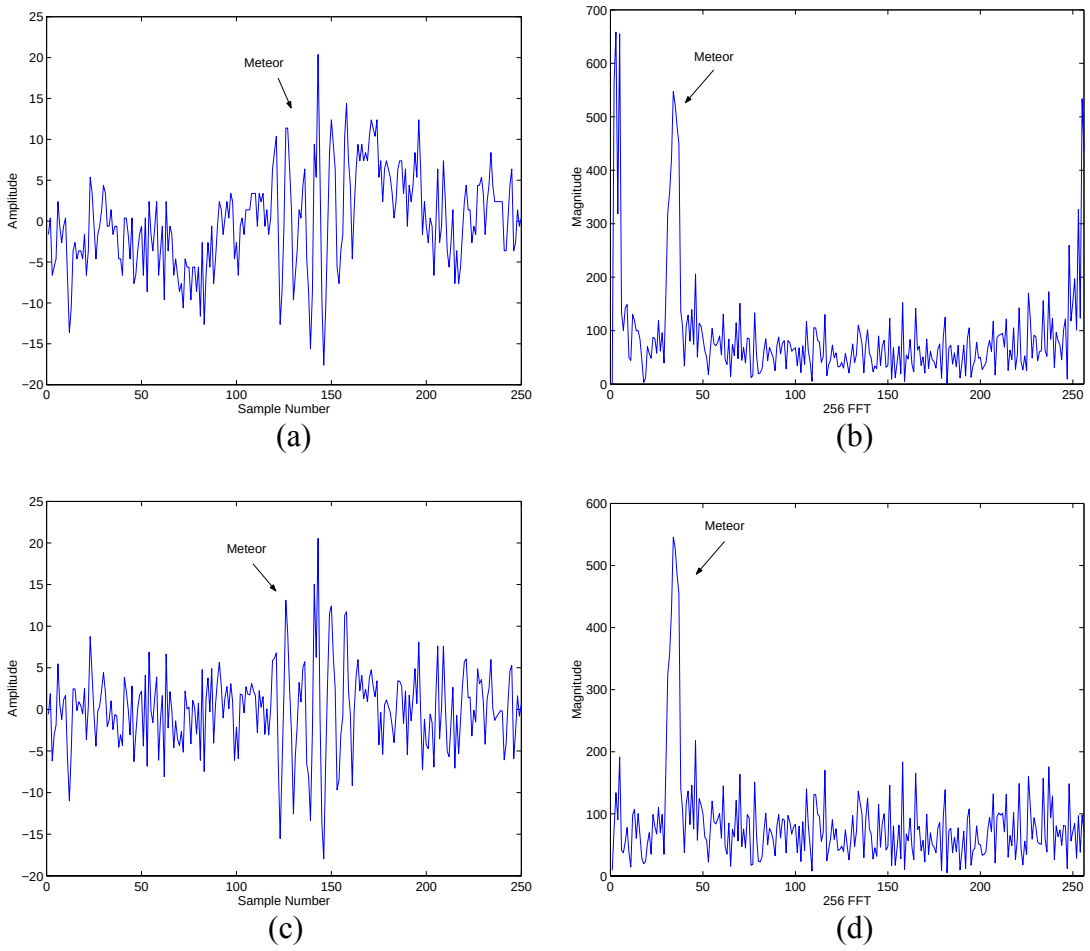

Figure 2.20: Results of applying the adaptive filter to the meteor event shown in Fig. 2.13(b). (a) and (b) are the real party of complex voltages of IPP #71 and its frequency spectrum. (c) and (d) are the output of the adaptive filter and its frequency spectrum.

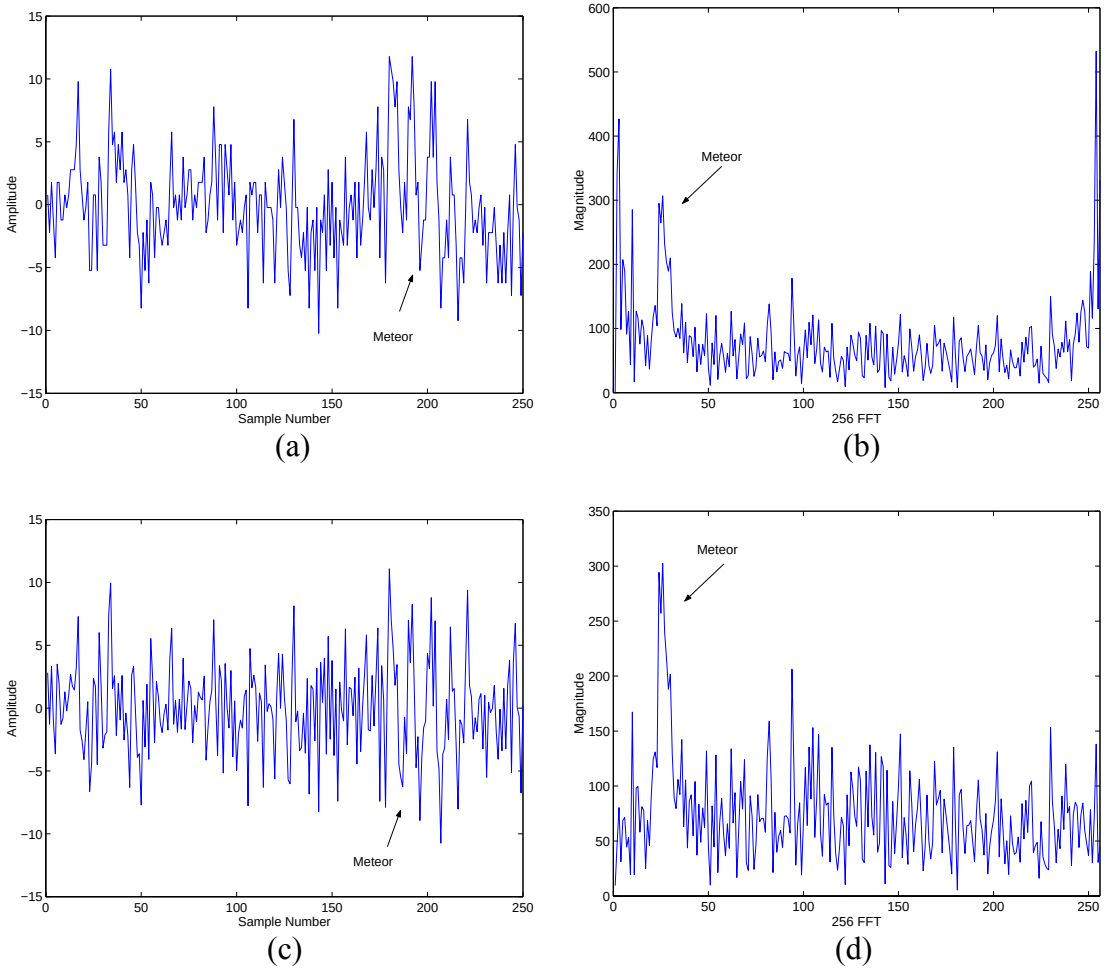

Figure 2.21: Results of applying the adaptive filter to the meteor event shown in Fig. 2.13(a). (a) and (b) are the real party of complex voltages of IPP #87 and its frequency spectrum. (c) and (d) are the output of the adaptive filter and its frequency spectrum.

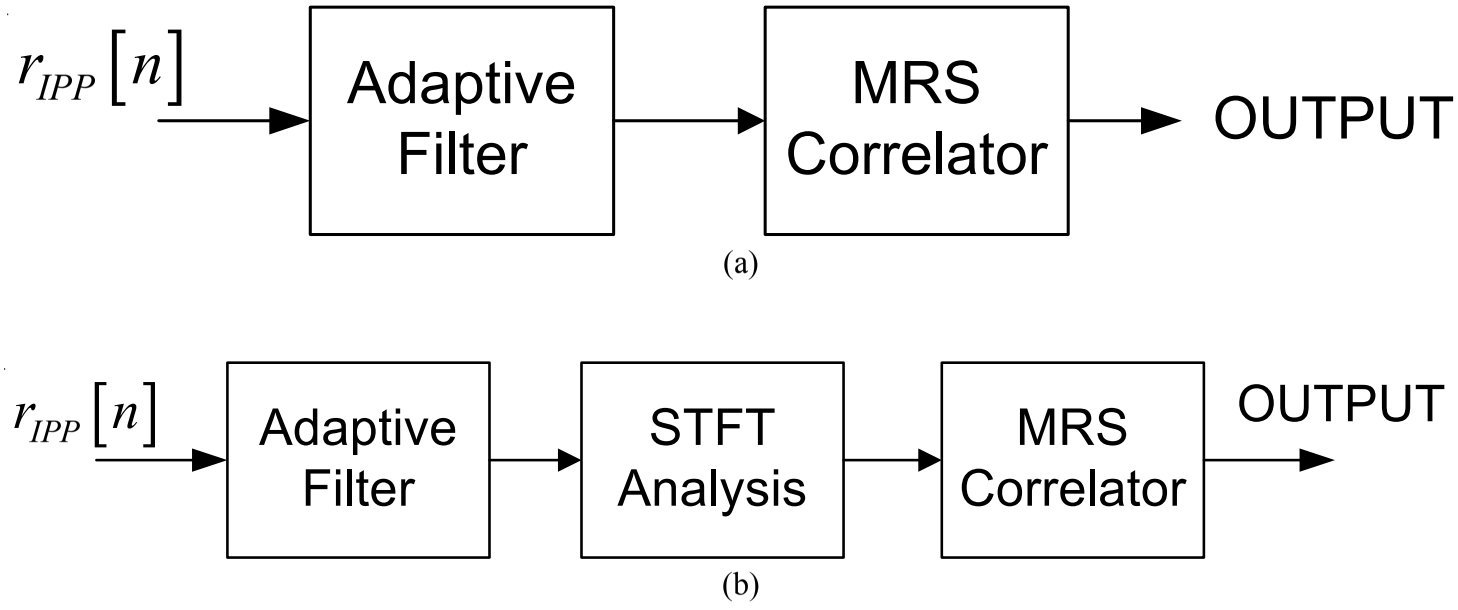

Figure 2.22: Flow charts of the experiments. (a) The combination of the adaptive filter and the MRS correlator. (b) The combination of the adaptive filter, the STFT analysis and the MRS correlator.

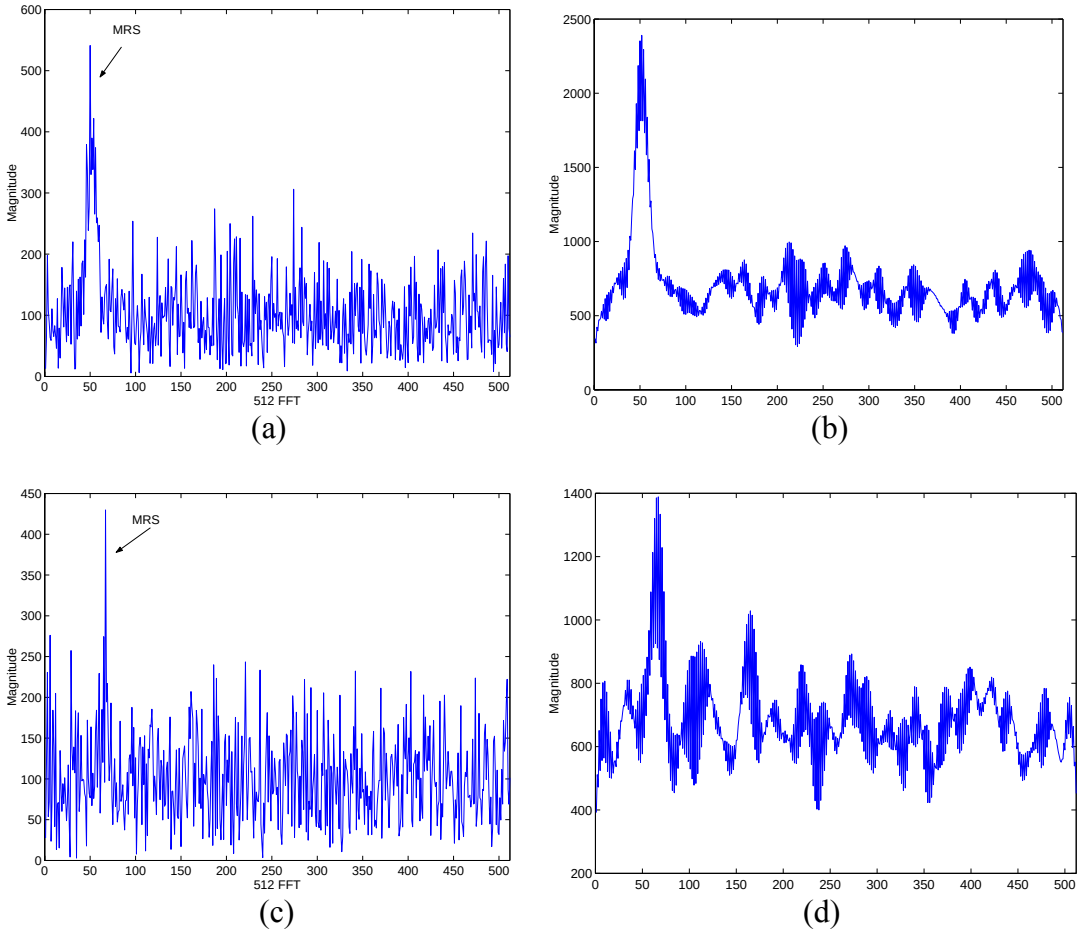

Figure 2.23: Experimental results of combining the adaptive filter and the MRS correlator. (a) and (b) are the frequency spectrum of the running window FFT containing IPP #87~#88 from the meteor event shown in Fig. 2.13(a) and the result of the MRS correlator. (c) and (d) are the frequency spectrum of the running window FFT containing IPP #127~#128 from the meteor event shown in Fig. 2.13(b) and the result of the MRS correlator.

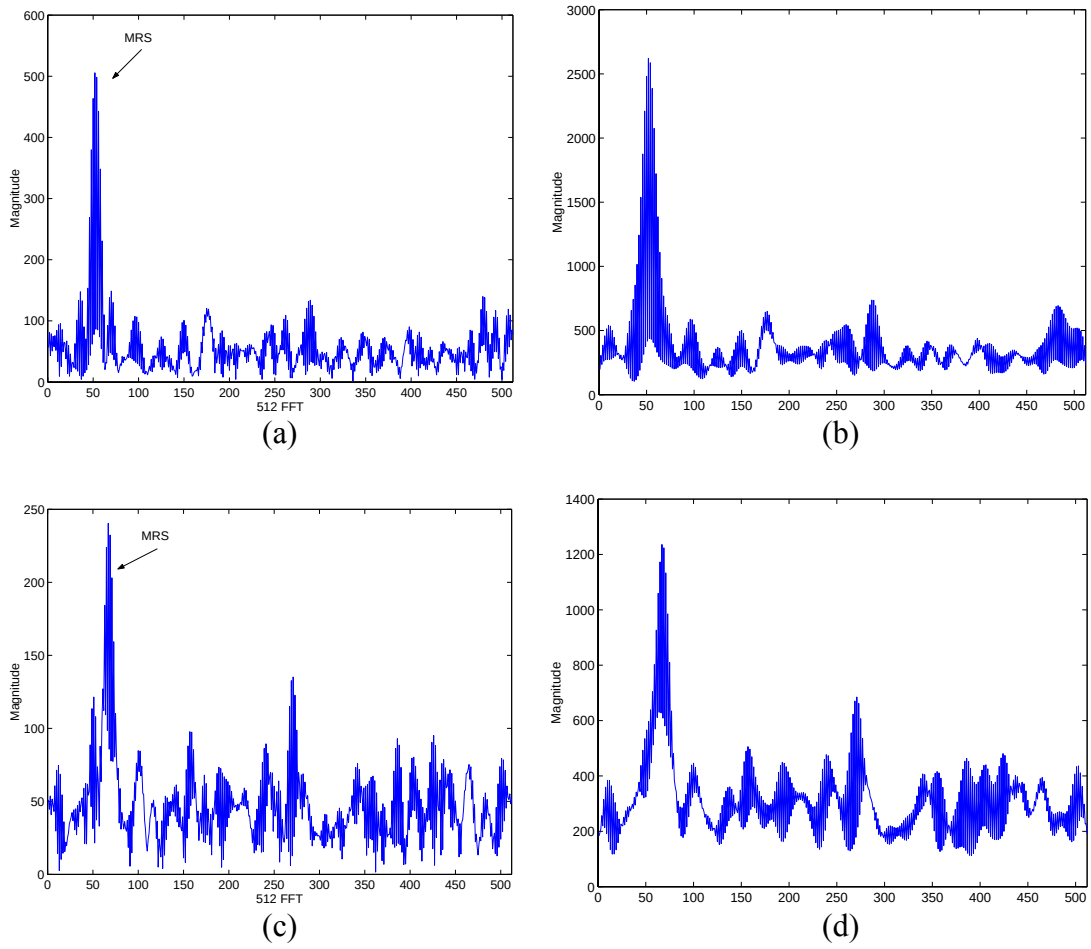

Figure 2.24: Experimental results of combining the adaptive filter, the STFT analysis and the MRS correlator. (a) The STFT analysis result of signal samples #183~#227 of IPP #87 and #88 from the meteor event shown in Fig. 2.13(a). (b) The result of the MRS correlator. The input is shown in part (a). (c) The STFT analysis result of signal samples #129~#173 of IPP #127 and #128 from the meteor event shown in Fig. 2.13(b). (d) The result of the MRS correlator. The input is shown in part (c).

Chapter 3

Interference Detection and Removal

The interference observed in AO meteor observation data could be separated into two categories: sparse or dense interference. Both of them are non-periodic and bursty (strong energy). Knowing these properties, we use signal processing techniques to detect and remove the interference samples in the meteor data. We introduce two interference detection methods. First, we calculate the central moments of the power profile of the meteor data (per IPP). When the fraction of the interference signal samples is very low (sparse interference), the kurtosis (4^{th} central moment) is very high. We detect the interference by calculating this parameter. Second, we apply a nonlinear filter to the power profile of the meteor data then calculate the power reduction percentage to detect the interference. After detecting the interference, we remove the corresponding interference signal samples.

We model the received signals in Section 3.1. Two detection methods are described in Section 3.2 and 3.3. The interference removal process is introduced in Section 3.4. Experimental results are given in Section 3.5.

3.1 Models for the Received Signals

The interference detection is performed IPP by IPP. Assume the received complex signal for each IPP is $r[n],\ n = 1, 2, ..., N_{IPP}$, where N_{IPP} is the number of signal samples per IPP. We normalize time, n, with respect to the sampling period for

notational convenience. The model for $r[n]$ consists of three different signals: (1) additive complex white noise, $n_w[n]$; (2) meteor return signal, $m[n]$; (3) interference signal, $i[n]$.

Let the real and imaginary part of $n_w[n]$ be $n_{w,r}[n]$ and $n_{w,i}[n]$, respectively. Both of them are Gaussian distributed random variables with mean 0 and variance σ^2, denoted by $N(0,\sigma^2)$.

The meteor return signal, $m[n]$, is modeled as

$$m[n] = A_M \exp\{j(\omega_D n + \phi)\} \Delta[n - l_M],\ n = 1, 2, ..., N_{IPP} \tag{3.1}$$

which is the same as (2.1). Note that we use A_M for the amplitude of meteor signal.

According to our observations, the energy of the interference is very strong and the duration is very short. We model the interference signal sample as

$$i[n] = A_{\text{int}} \exp\{j\theta\} \delta[n] \tag{3.2}$$

where A_{int} is the amplitude, θ is the phase, and $\delta[n]$ is the unit sample function. There may be several interference samples in one IPP. To simplify the analysis, we assume all interference samples within one IPP have the same amplitude.

When all three signals are present in one IPP, $r[n]$ is expressed as

$$r[n] = n_w[n] + m[n] + \sum_{i=1}^{N_{\text{int}}} i[n - p_i],\ n = 1, 2, ..., N_{IPP} \tag{3.3}$$

where N_{int} is the number of interference samples, and p_i is the position of i-th interference sample, which is assumed uniformly distributed between 1 and N_{IPP}.

The power profile of $r[n]$ in (3.3) is expressed as

$$P_r[n] = \left|n_w[n]\right|^2 + \left|m[n]\right|^2 + \sum_{i=1}^{N_{\text{int}}} \left|i[n-p_i]\right|^2,\ n = 1,2,...,N_{IPP} \tag{3.4}$$

Substituting (3.1) and (3.2) into (3.4), we have

$$P_r[n] = \left|n_w[n]\right|^2 + A_M^2 \Delta\left[n - l_M\right] + \sum_{i=1}^{N_{\text{int}}} A_{\text{int}}^2 \delta[n-p_i],\ n = 1,2,...,N_{IPP} \tag{3.5}$$

Note that $P_r[n]$ is always real and non-negative. We will use $P_r[n]$ to detect the presence of the interference.

3.2 Interference Detection: Nonlinear Filter Method

To detect the presence of the interference we first apply a minimum filter of window size 5 to $P_r[n]$. Note that the window size of the minimum filter must be larger than the duration of one interference, otherwise this method does not work. The output of the minimum filter, $P_{r,\min}[n]$, is expressed as

$$P_{r,\min}[n] = \min\left\{P_r[n-2], P_r[n-1], P_r[n], P_r[n+1], P_r[n+2]\right\},\ n = 1,2,...,N_{IPP} \tag{3.6}$$

We ignore samples with indices outside the range $1 \le n \le N_{IPP}$. We then calculate the standard deviation of $P_r[n]$ and the power reduction percentage (PRP), which is defined by

$$PRP = \frac{\sum_{n=1}^{N_{IPP}} \left(P_r[n] - P_{r,\min}[n]\right)}{\sum_{n=1}^{N_{IPP}} P_r[n]} \times 100\% \tag{3.7}$$

Using these two parameters (standard deviation and PRP) we can identify the presence of interferences. We evaluate these two parameters for three different cases.

Case I: $r[n]$ consists of additive white Gaussian noise only

Without the presence of the meteor and the interference signals, $P_r[n],\ n=1,2,...,N_{IPP}$ are independent and identical chi-square distributed random variables with 2 degrees of freedom [17]. The probability density function (PDF), $f_p(x)$, and the cumulative density function (CDF), $F_p(x)$, of $P_r[n]$ are [10]

$$f_P(x)=\frac{1}{2\sigma^2}\exp\left\{-\frac{x}{2\sigma^2}\right\},\ x\geq 0 \tag{3.8}$$

$$F_P(x)=1-\exp\left\{-\frac{x}{2\sigma^2}\right\},\ x\geq 0 \tag{3.9}$$

The expected value and standard deviation of $P_r[n]$ are

$$E\left\{P_r(n)\right\}=2\sigma^2 \tag{3.10}$$

$$Std\left\{P_r(n)\right\}=2\sigma^2 \tag{3.11}$$

To derive the probability density function of $P_{r,\min}[n]$, we define $R_P(x)=\text{Prob}\left\{P_r[n]>x\right\}$. Then

$$R_{P,\min}(x)=\text{Prob}\left\{P_{r,\min}[n]>x\right\}=\text{Prob}\left\{P_r[n-k]>x\right\},\ k=-2,-1,...,2 \tag{3.12}$$

Use the independent and identically distributed property, (3.12) becomes

$$R_{P,\min}(x)=\left(\text{Prob}\left\{P_r[n]>x\right\}\right)^5=R_P^5(x) \tag{3.13}$$

Note that $R_P(x)=1-F_p(x)$. The derivative of (3.13) is then

$$\frac{d}{dx}R_{P,\min}(x)=-f_{P,\min}(x)=-5f_P(x)R_P^4(x) \tag{3.14}$$

Substituting (3.8), (3.9) into (3.14), we have

$$f_{P,\min}(x) = \frac{5}{2\sigma^2}\exp\left\{-\frac{5x}{2\sigma^2}\right\},\ x \geq 0 \tag{3.15}$$

The expected value of $P_{r,\min}[n]$ is

$$E\left\{P_{r,\min}[n]\right\} = \frac{2}{5}\sigma^2 \tag{3.16}$$

Substituting (3.10), (3.16) into (3.7), we have the expected value of PRP.

$$E\left\{PRP\right\} = \frac{\sum_{n=1}^{N_{IPP}}\left(E\left\{P_r[n]\right\} - E\left\{P_{r,\min}[n]\right\}\right)}{\sum_{n=1}^{N_{IPP}} E\left\{P_r[n]\right\}} \times 100\% = \frac{2\sigma^2 - \frac{2}{5}\sigma^2}{2\sigma^2} = 80\% \tag{3.17}$$

Case II: $r[n]$ consists of white Gaussian noise and meteor return signals

In this case, $P_r[n],\ n = l_M, l_M + 1, ..., l_M + 44$, corresponding to the meteor return signals, are independent and identical noncentral chi-square distributed random variables with 2 degrees of freedom with noncentrality parameter A_M^2; other samples are independent and identical chi-square distributed random variables with 2 degrees of freedom. The PDF of $P_r[n]$ is modeled as

$$f_P(x) = p \cdot f_N(x) + q \cdot f_M(x) \tag{3.18}$$

where $q = 45 / N_{IPP}$, $p + q = 1$, $f_N(x)$ is the PDF of chi-square distribution expressed in (3.8), and $f_M(x)$ is the PDF of noncentral chi-square distribution, i.e.,

$$f_M(x) = \frac{1}{2\sigma^2}\exp\left\{-\frac{\left(A_M^2 + x\right)}{2\sigma^2}\right\} I_0\left(\sqrt{x}\frac{A_M}{\sigma^2}\right),\ x \geq 0 \tag{3.19}$$

where $I_0(.)$ is 0^{th} order modified Bessel function. The expected value and standard deviation of $P_r[n]$ are

$$E\{P_r[n]\} = 2\sigma^2 p + A_M^2 q \tag{3.20}$$

$$Std\{P_r[n]\} = \sqrt{4\sigma^4 + 4\sigma^2 A_M^2 q + A_M^4 pq} \tag{3.21}$$

To evaluate the PRP, we consider the very high SNR meteor return signal case first. For this case, the noise power is negligible when calculating the PRP, and the power of meteor signals are approximately equal to a constant, that is

$$P_r[n] \cong \begin{cases} A_M^2, & n = l_M, l_M + 1, ..., l_M + 44 \\ 2\sigma^2, & n \neq l_M, l_M + 1, ..., l_M + 44 \end{cases} \tag{3.22}$$

After applying the minimum filter, the resultant $P_{r,\min}[n]$ is

$$P_{r,\min}(n) \cong \begin{cases} A_M^2, & n = l_M + 2, l_M + 3, ..., l_M + 42 \\ \frac{2}{5}\sigma^2, & n \neq l_M + 2, l_M + 3, ..., l_M + 42 \end{cases} \tag{3.23}$$

Note that after applying the minimum filter with window size 5, we lose 4 samples at the beginning and the end of the meteor return signals. The approximate PRP is

$$PRP \cong \frac{45A_M^2 - 41A_M^2}{45A_M^2} \times 100\% \cong 9\% \tag{3.24}$$

For lower SNR case the PRP will be larger than 9% but less than 80% (no meteor return signals).

Case III: $r[n]$ consists of noise and interference signals

We assume the interference signals in the same IPP have the same power, i.e., $P_r[n] = A_{\text{int}}^2$, $n \in \{\text{interference signal samples}\}$. Other power profile file samples are chi-

square distributed reandom variables with 2 degrees of freedom. The PDF of $P_r[n]$ is modeled as

$$f_P(x) = p \cdot f_N(x) + q \cdot f_I(x) \tag{3.25}$$

where $q = N_{\text{int}} / N_{IPP}$, $p = 1 - q$, N_{int} is the number of interference signal samples, $f_N(x)$ is the same as in (3.18), and $f_I(x) = \delta[x - A_{\text{int}}^2]$. The expected value and standard deviation of $P_r[n]$ are

$$E\{P_r[n]\} = 2\sigma^2 p + A_{\text{int}}^2 q \tag{3.26}$$

$$Std\{P_r[n]\} = \sqrt{8\sigma^4 p + A_{\text{int}}^4 q - \left(2\sigma^2 p + A_{\text{int}}^2 q\right)^2} \tag{3.27}$$

Note that A_{int}^2 is much larger than σ^2, so the dominant term for standard deviation is $A_{\text{int}}^4 q$, which is proportional to *q* (the fraction of interference samples in one IPP).

Since the window size of the minimum filter is larger than the duration of the interference, $P_{r,\min}[n]$ is approximately equeal to the one derived in the noise only case, i.e., (3.12)~(3.16). The expected value of PRP is

$$E\{PRP\} = \frac{\sum_{n=1}^{N}\left(E\{P_r[n]\} - E\{P_{r,\min}[n]\}\right)}{\sum_{n=1}^{N} E\{P_r[n]\}} \times 100\% = \frac{\left(2p - 2/5\right)\sigma^2 + A_I^2 q}{2\sigma^2 p + A_I^2 q} \times 100\% \tag{3.28}$$

Note that PRP is also proportional to *q*. So the smallest PRP occurs when there is only one interference sample, i.e., $q = 1/N_{IPP}$. According to our observations, A_{int}^2 is always larger than $1000\sigma^2$; and the typical meteor observation data contains 250 signal samples per IPP. Using $A_{\text{int}}^2 = 1000\sigma^2$ and $q = 1/250$, the expected $P_r[n]$ and PRP are

equal to $63\sigma^2$ and 93%, which are much larger compared to those without the presence of the interference.

Fig. 3.1 shows the scatter plot of more than 2000 IPPs using the two parameters. These results include all three cases we mentioned above. They match the mathematical derivations very well. The interference IPPs can be detected by applying appropriate thresholds.

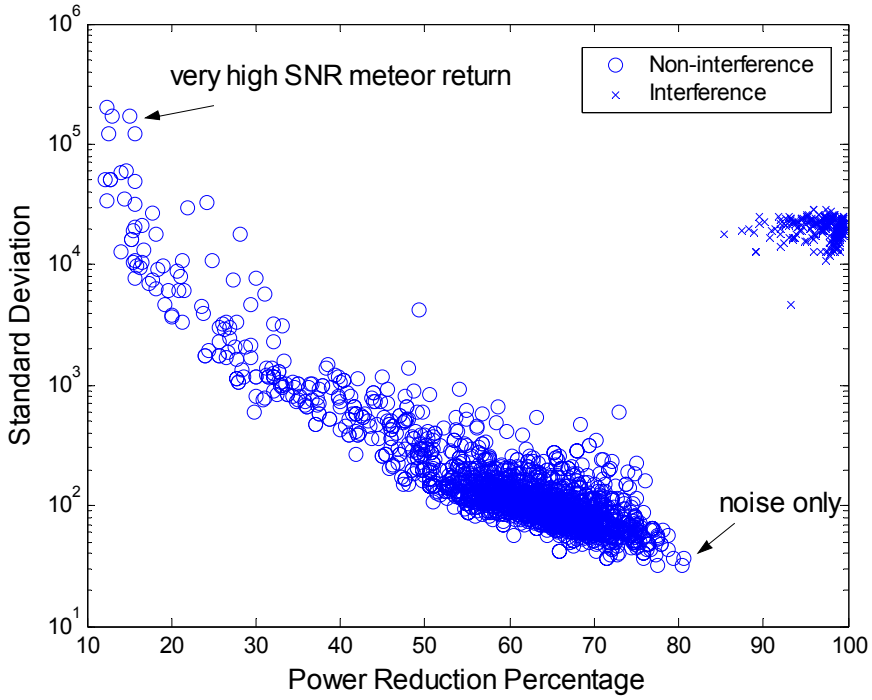

Figure 3.1: The representation of 2281 non-interference and 320 interference IPPs using standard deviation and power reduction percentage as two parameters. We can use thresholds to easily distinguish the interference IPPs.

3.3 Interference Detection: Kurtosis Method

When the fraction of interference samples in one IPP is very small, we can use a simple kurtosis method to detect the presence of the interference. Assume the received signal, $r[n]$, consists of additive white noise and the interference. Using the signal model of (3.25), we have

$$E\left\{\left(P_r[n]-E\left\{P_r[n]\right\}\right)^4\right\}=384\sigma^8+A_{\text{int}}^8 q-\left(144\sigma^6 p+A_{\text{int}}^6 q\right)\left(2\sigma^2 p+A_{\text{int}}^2 q\right)+\left(48\sigma^4 p+A_{\text{int}}^4 q\right)\left(2\sigma^2 p+A_{\text{int}}^2 q\right)^2-3\left(2\sigma^2 p+A_{\text{int}}^2 q\right)^4 \tag{3.29}$$

Using (3.26) and (3.29), we can calculate the kurtosis.

Fig. 3.2 shows the kurtosis vs. the fraction of interference samples in one IPP. The interference-to-noise ratio is 1000. Note that when the fraction is less than 1% the kurtosis is very high. Fig. 3.3 shows one example of AO data recorded at 18:30:11.153 AST 17 October 1998 with sparse interference and the kurtosis of each IPP. The kurtosis is very high when the sparse interference appears in the IPP. Using this property, we detect the presence of the sparse interference.

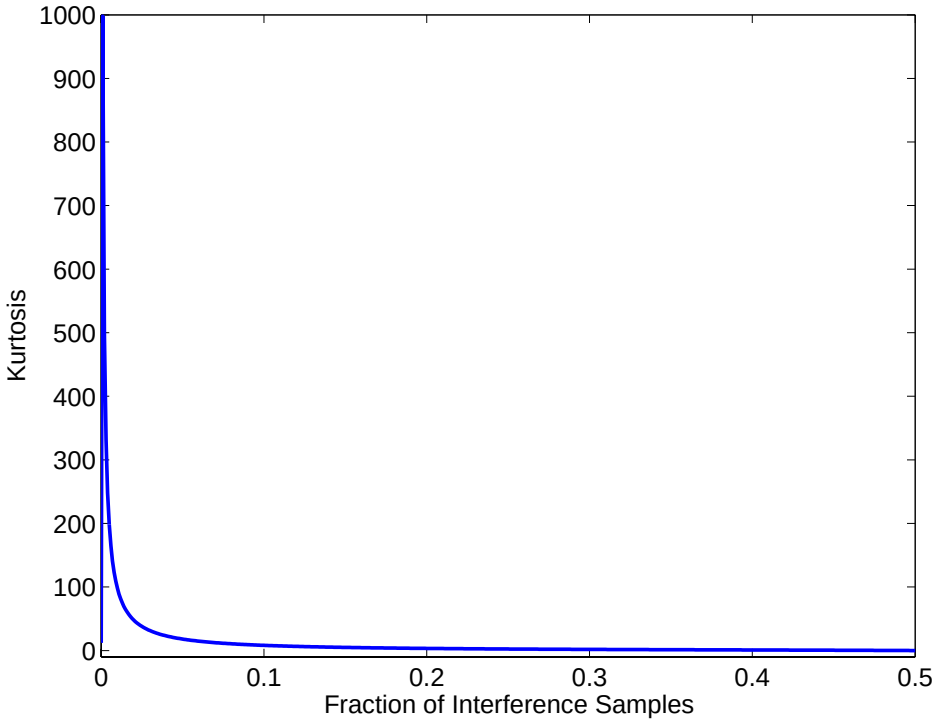

Figure 3.2: Kurtosis vs. the fraction of interference samples in one IPP

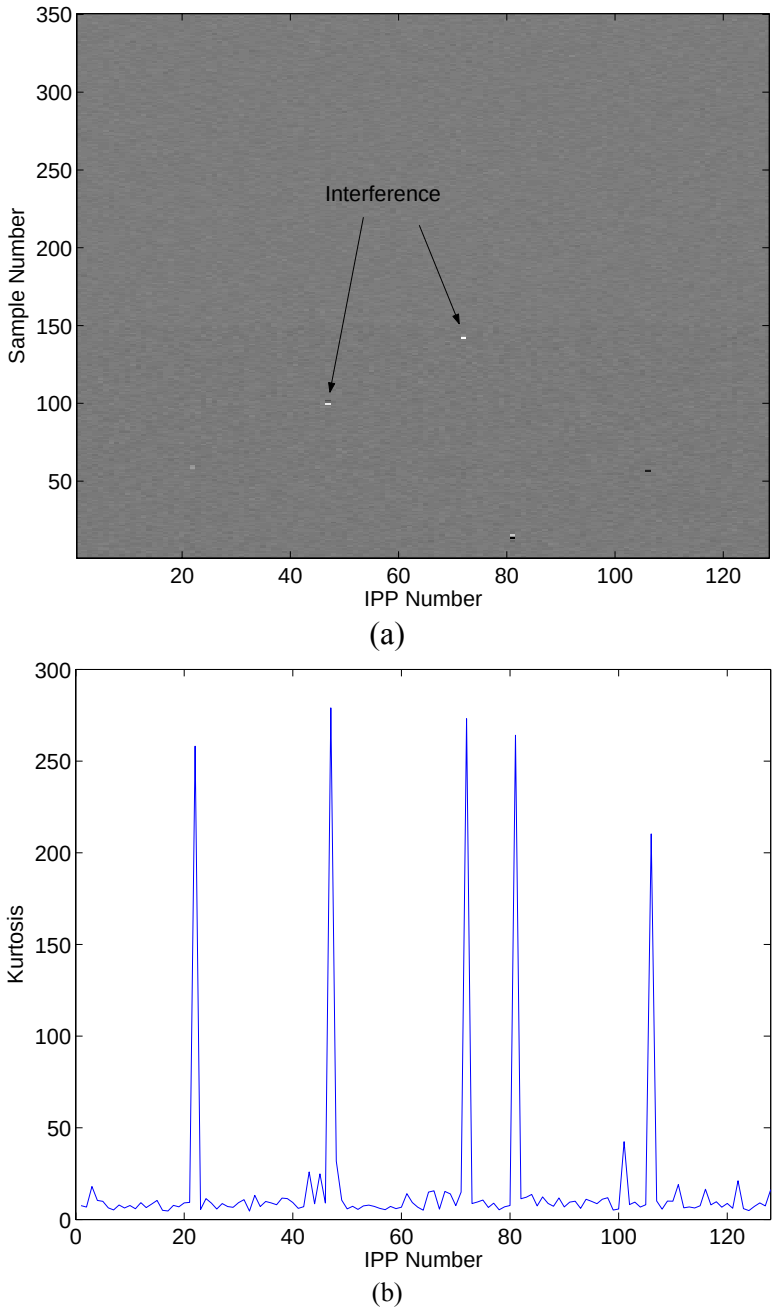

Figure 3.3: An example of the kurtosis method (a) One example of the sparse interferences in the meteor observation data recorded at 18:30:11.153 AST 17 Oct. 1998. We can see few interference signal samples in the image. (b) The kurtosis of each IPP shown in part (a).

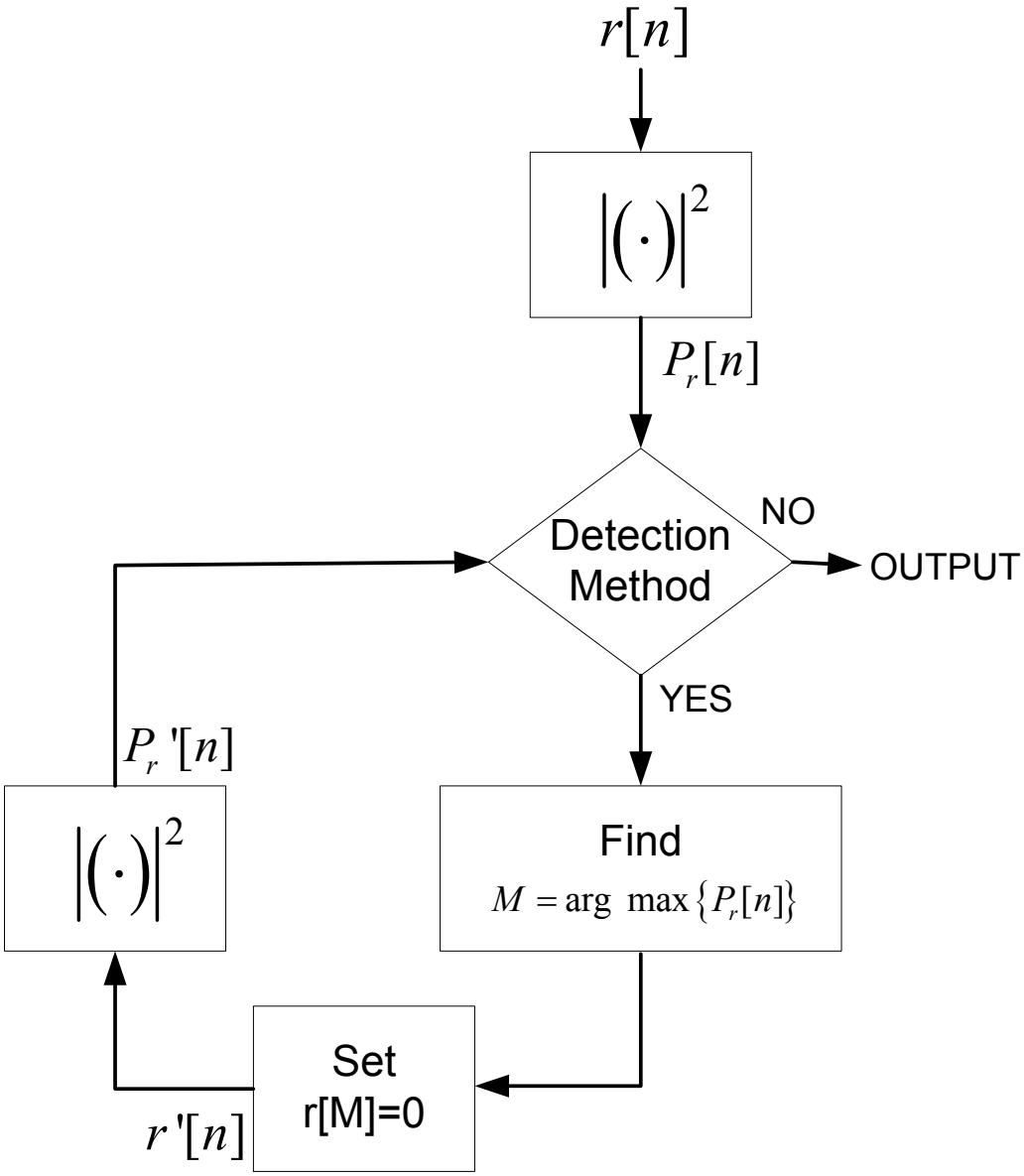

Figure 3.4: Flow chart of the interference removal process.

3.4 Interference Removal Process

After detecting the interference signals, we blank one signal sample with maximal energy in the IPP. We then apply the detection mechanism to the resultant IPP again to see if there is any residual interference. If yes, we blank one signal sample with maximal energy. We recursively do this process until it passes the interference detection test. Fig. 3.4 shows the flow chart of interference removal. The detection method in the flow chart could be the nonlinear filter method or the kurtosis method or the combination of the two methods.

3.5 Experimental Results

In this section we demonstrate some experimental results of interference removal. We first use real meteor observation data from Arecibo Observatory to show the result of interference removal. We then synthesize the IPP signals containing both meteor and interference and use them to show the performance of the combination of interference removal and meteor detection algorithms. Fig. 3.5 shows the experimental result of the sparse interference removal. The interference data is the same as the data shown in Fig. 3.3. For this kind of interference, both kurtosis and nonlinear filter methods can detect its presence. We use kurtosis method here and set the threshold to be 50. Fig. 3.5 (a) and (b) show the image, which consists of 128 IPPs, of the real part of the complex voltage of the meteor observation data and the power profile of IPP #81 containing an interference, respectively. Fig. 3.5 (c) and (d) show the results of the interference removal of part (a) and (b), respectively. Note that the bursty interference is removed by the algorithm.

Fig. 3.6 shows one example of the dense interference recorded at 06:57:13.560 AST 11 August 2002. Fig. 3.6 (a) and (b) are the real part of the complex voltage of the IPP signals and the power profile of IPP #33, respectively. We can see many spiky interference signals here. Fig. 3.6 (c) and (d) show the results of interference removal using the nonlinear filter method of part (a) and (b), respectively. We set the standard deviation and the power reduction percentage equal to 1000 and 75% as the thresholds. The interference signal samples are completely removed in this example. Note that the kurtosis method does not work for dense interference case because the fraction of the interference samples in one IPP is too high.

Fig. 3.7 (a) shows the real part of complex voltage of one synthetic meteor data. We insert the prototype meteor event into the dense interference to examine the performance of the interference removal mechanism. Fig. 3.7 (b) shows the result. We use the nonlinear filter method to detect the interference and set standard deviation and power reduction percentage equal to 1000 and 75%, respectively. We can see the algorithm removes most of the interference signals. Fig. 3.7 (c) shows one example of the IPP containing both meteor and interference signals; and Fig. 3.7 (d) shows the result after interference removal. Fig. 3.7 (e) and (f) show the frequency spectrum of the window containing IPP #51~54 before and after the interference removal. Comparing Fig. 3.7 (e) and (f), we can see that it is much easier to detect the meteor after the interference removal process. Note that there is a residual interference in IPP #53 as shown in Fig. 3.7 (d), which doesn't affect the meteor detection. Also note that when the interference and meteor signals coincide, the algorithm will remove those samples, which will degrade the performance of meteor detection.

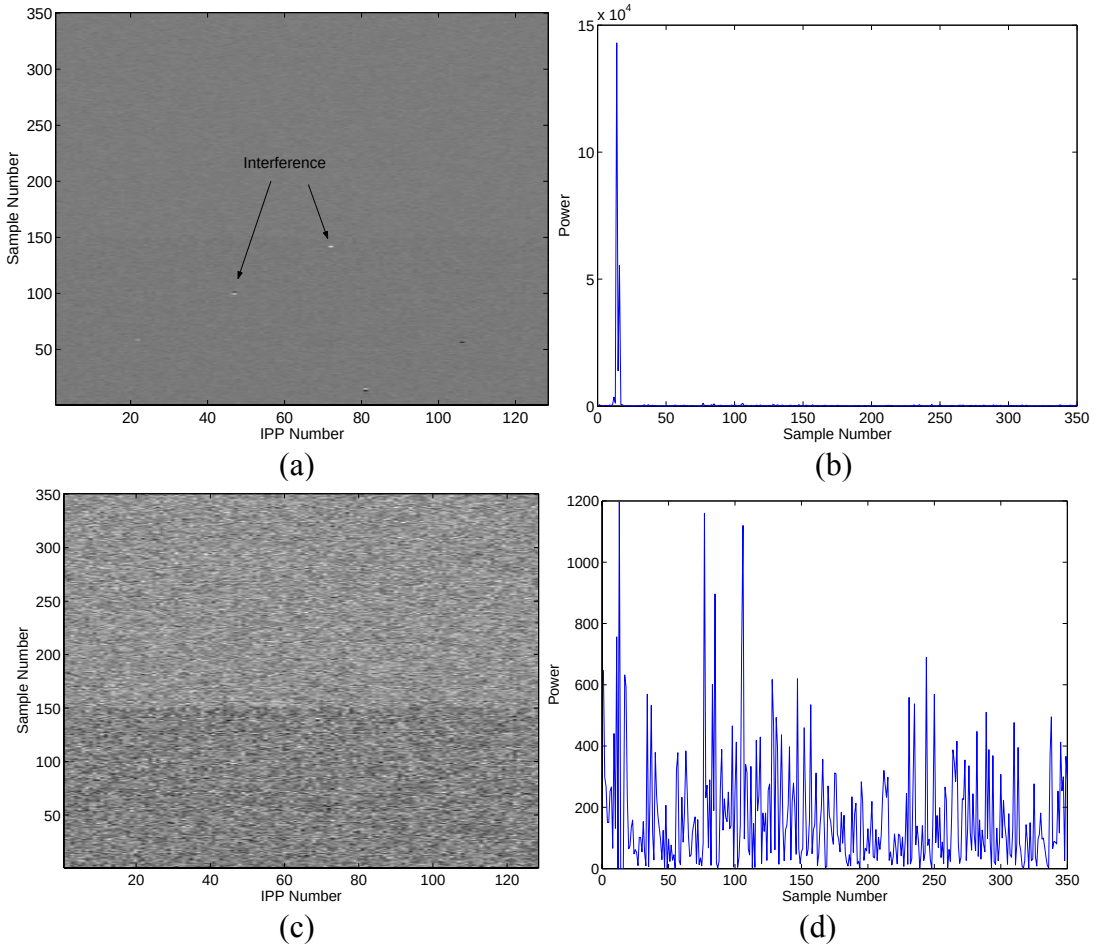

Figure 3.5: One example of the sparse interference removal. (a) The sparse interference. (b) Power profile of IPP #81. (c) The result of interference removal of part (a). (d) The power profile of IPP #81 after interference removal.

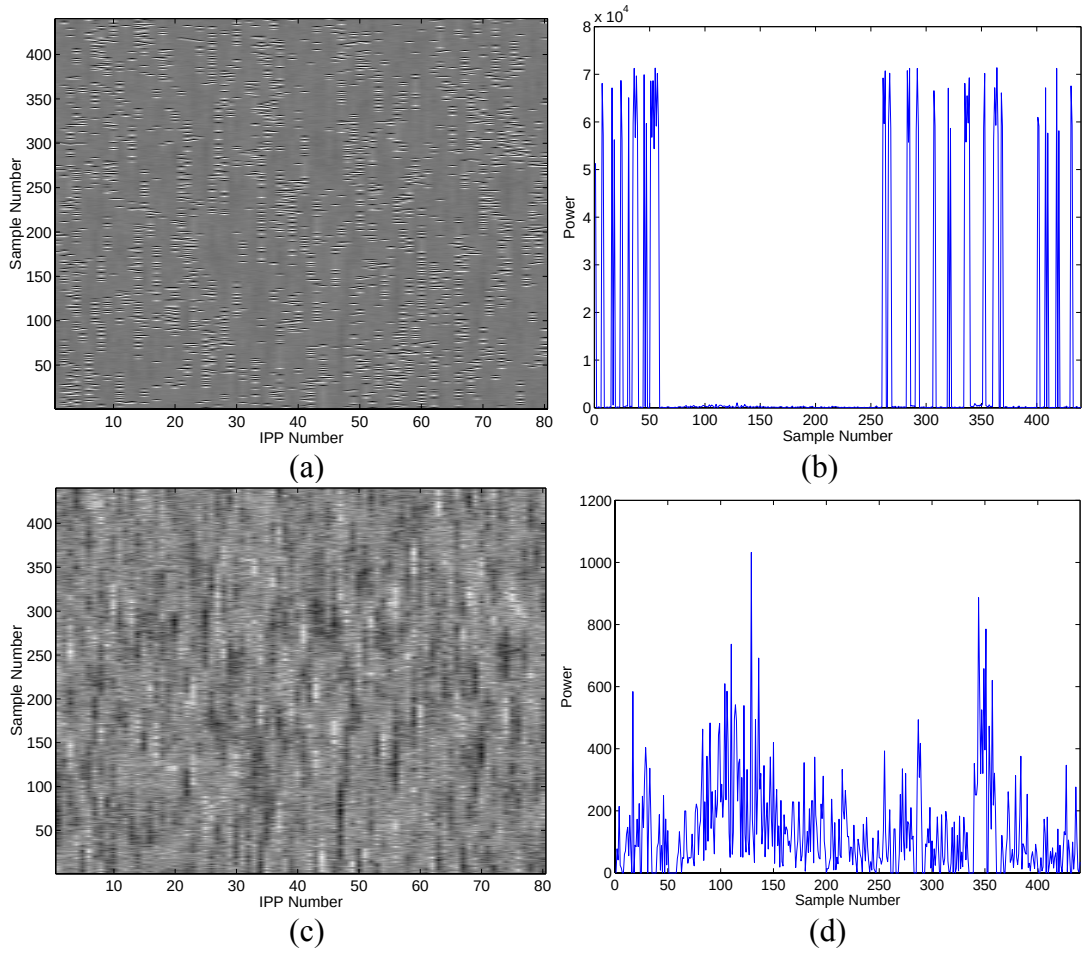

Figure 3.6: One example of dense interference removal. (a) The real part of complex voltage of the dense interference recorded at 06:57:13.560 AST 11 Aug. 2002. (b) The power profile of IPP #33. (c) The result of interference removal of part (a). (d) The power profile of IPP #33 after interference removal.

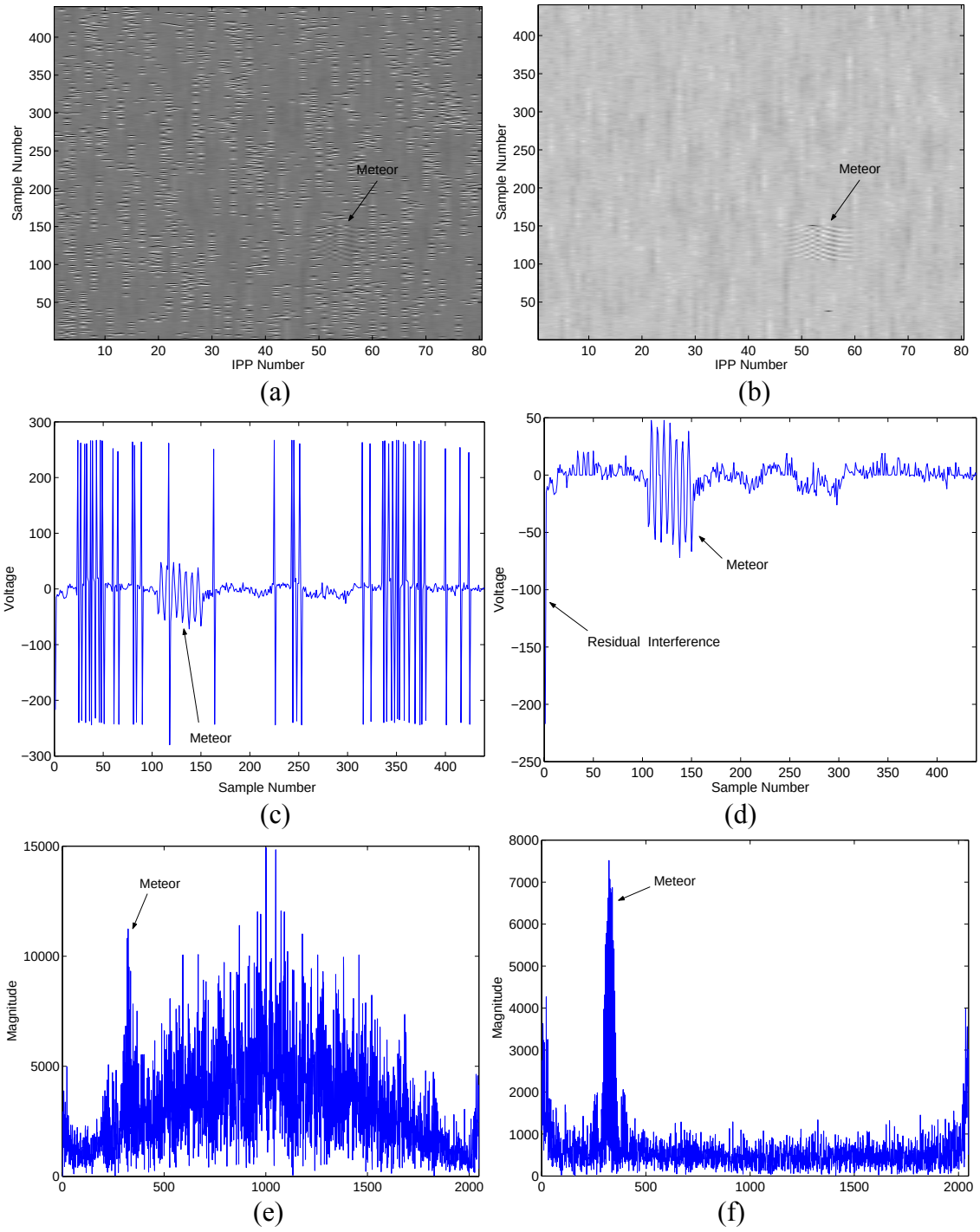

Figure 3.7: One example of the combination of the interference removal and the meteor detection (a) Synthetic meteor data with interferences. (b) The result of interference removal of (a). (c) Real part of the complex voltage of IPP #53 in (a). (d) The result of the interference removal of (c). (e) The frequency spectrum of the window containing IPPs #51~#54 in (a). (f) The frequency spectrum of the window containing IPPs #51~#54 in (b).

Chapter 4

Ionosphere Observation Data

The Arecibo 430 MHz Incoherent Scatter Radar (ISR) has been used to observe the ionosphere and meteors over forty years. Currently the ISR ionosphere observations are made using 13-baud Barker or 88-baud pseudo-random coded pulses. The meteor signals have traditionally been treated as the interference in ionosphere observation data. In this chapter we present signal processing techniques that separate these two different signals into different geophysically interesting data sets. We use a filterbank followed by the short time Fourier transform (STFT) analysis to remove the meteor signals from the incoherent scatter results. By doing this the incoherent scatter data will not be contaminated and we can also analyze meteor characteristics from the separated signal. We also use similar interference removal techniques described in Chapter 3 to remove the interference signal. Some experimental results are given in this chapter.

4.1 Separation of Meteor and Incoherent Scatter Signals

The ISR ionosphere observations are made using Barker coded carrier pulses with the inter-pulse period (IPP) of 10 milliseconds. The received signals are mixed to base-band (DC center frequency) and then sampled in in-phase and quadrature-phase channels. To separate the incoherent scatter and the meteor signals, we first use a filterbank to detect the meteor then use STFT analysis to remove the meteor signals.

Let the received signals of one IPP be

$$r_{coded}[n],\ n=1,2,...,N \tag{4.1}$$

where N is the number of samples and let the code be

$$c_{\text{code}}=\left[c[1],c[2],\cdots,c[M]\right] \tag{4.2}$$

where M is the code length. The decoded result, a voltage, is written as

$$r_{decoded}[n]=\sum_{k=1}^{M} r_{coded}[n+k-1]c[k],\ n=1,2,...,N \tag{4.3}$$

Notice that the decoded result can be found in transform domain as is done in practice. Because of the Doppler speed of the meteor, the decoding process effectively uses the wrong code thus spreading the meteor energy over a sample twice interval the code length, which deteriorates the result. Fig. 4.1(a) shows the power profiles of the decoded signals recorded at 22:20:22.990, September 3rd, 2001. A 13 baud Barker code was used. There is one meteor event in this sequence. Fig. 4.1(b) shows the power profile of the raw undecoded signal of that meteor event; and Fig. 4.1(c) shows the power profile of the decoding result using (4.3). In Fig. 4.1(c) the meteor energies spread in range because it is not decoded correctly, i.e., the decoding assumed zero Doppler offset. To properly decode meteor signals we need to correct the code for the Doppler offset that results in a complex-valued code. The modified decoding equation after multiplication by the appropriate phasor is

$$r_{meteor}[n]=\sum_{k=1}^{M} r_{coded}[n+k-1]c[k]e^{-j\omega_D kT} \tag{4.4}$$

where ω_D is the Doppler frequency of the meteor, and T is the sampling period. Fig. 4.1(d) shows the decoding result using the correct Doppler frequency shifted Barker code. Note that the decoding result for incoherent scatter signals is now erroneous. The

figure shows that we can detect the presence of the meteor with proper threshold and precisely identify the location of the meteor.

After identifying the meteor, we use the STFT to analyze the corresponding meteor signals. We use the data shown in Fig. 4.1(b) to illustrate the process. For this data set a 13-baud Barker coded pulse was transmitted. With this prior knowledge and the meteor location identified by the Doppler frequency shifted Barker decoder, we get the Barker coded meteor signals. Let the coded noise free meteor signals be $r_{coded}[L]$, $r_{coded}[L+1],\ldots,\ r_{coded}[L+12]$, where L is the range gate location of the meteor. Each meteor signal sample is modeled by

$$r_{coded}[L-1+n] = Ae^{j(\omega_D nT+\phi)}c[n],\ n=1,2,...,13 \tag{4.5}$$

where A is the amplitude, ω_D is the Doppler frequency of the meteor signals, T is the sampling period, ϕ is the phase, and

$$c_{\text{Barker},13} = \left[c[1],c[2],...,c[13]\right] = [1,1,1,1,1,-1,-1,1,1,-1,1,-1,1] \tag{4.6}$$

is the 13 Barker code. The STFT of the meteor signals is

$$\begin{aligned} M\left[k\right] &= \text{FFT}\left\{\left[r_{coded}[L]\cdot c[1], r_{coded}[L+1]\cdot c[2],..., r_{coded}[L+12]\cdot c[13]\right]\right\} \\ &= \text{FFT}\left\{\left[\begin{array}{l} Ae^{j(\omega_D T+\phi)}\cdot c[1]\cdot c[1], Ae^{j(2\omega_D T+\phi)}\cdot c[2]\cdot c[2],..., \\ Ae^{j(13\omega_D T+\phi)}\cdot c[13]\cdot c[13] \end{array}\right]\right\} \\ &= \text{FFT}\left\{\left[Ae^{j(\omega_D T+\phi)}, Ae^{j(2\omega_D T+\phi)},..., Ae^{j(13\omega_D T+\phi)}\right]\right\} \end{aligned} \tag{4.7}$$

Note that $c[n]\cdot c[n]=1,\ n=1,2,...,13$. We use fast Fourier transform (FFT) to calculate the frequency spectrum of the meteor signals. Note that we can zero pad the signals to get more spectrum samples. Fig. 4.2(a) shows the original coded received meteor signals. The signals after multiplying the 13 Barker code are shown in Fig. 4.2(b). We

can clearly see a sinusoidal signal in Fig. 4.2(b). The frequency corresponds to the speed of the meteor. Equation (4.7) is the frequency spectrum of a sinusoidal signal. If we zero pad the signals, we have a sinc function in frequency domain. Fig. 4.3 shows the magnitude of the STFT of the meteor event shown in Fig. 4.1(a). We can clearly see the meteor energy (sinc function) in the frequency spectrum. To remove the meteor signals we use the spectrum to estimate the frequency spectrum of meteor signals (sinc function) and then subtract it from the original spectrum. Fig. 4.4(a) shows the power profile of the undecoded IPP with meteor removal. Fig. 4.4(b) shows the power profile of the decoded result, the process removes 90% of the meteor signal energy. Fig. 4.4(c) shows RTI plot of the Fig. 4.1 results with the meteor return removed.

Fig. 4.5 shows the flowchart of the meteor signal detector and removal. This figure summarizes the process we just discussed. The input is one IPP signal at a time – when running a meteor observation program we analyze 4 or more IPPs at a time [5]. Since we don't know the Doppler frequency of the meteor signals a priori, we construct a filterbank. Each filter of the filterbank is a Barker decoder with different Doppler frequency shift. The filter that produces the maximum peak gives the best estimation of the meteor Doppler frequency. We can increase the resolution of Doppler frequency estimation by adding more filters. A threshold detector follows the filterbank. When at least one output of the filters exceeds the threshold we declare meteor detection. We then remove the meteor signals by STFT analysis, e.g. Fig. 4.3.

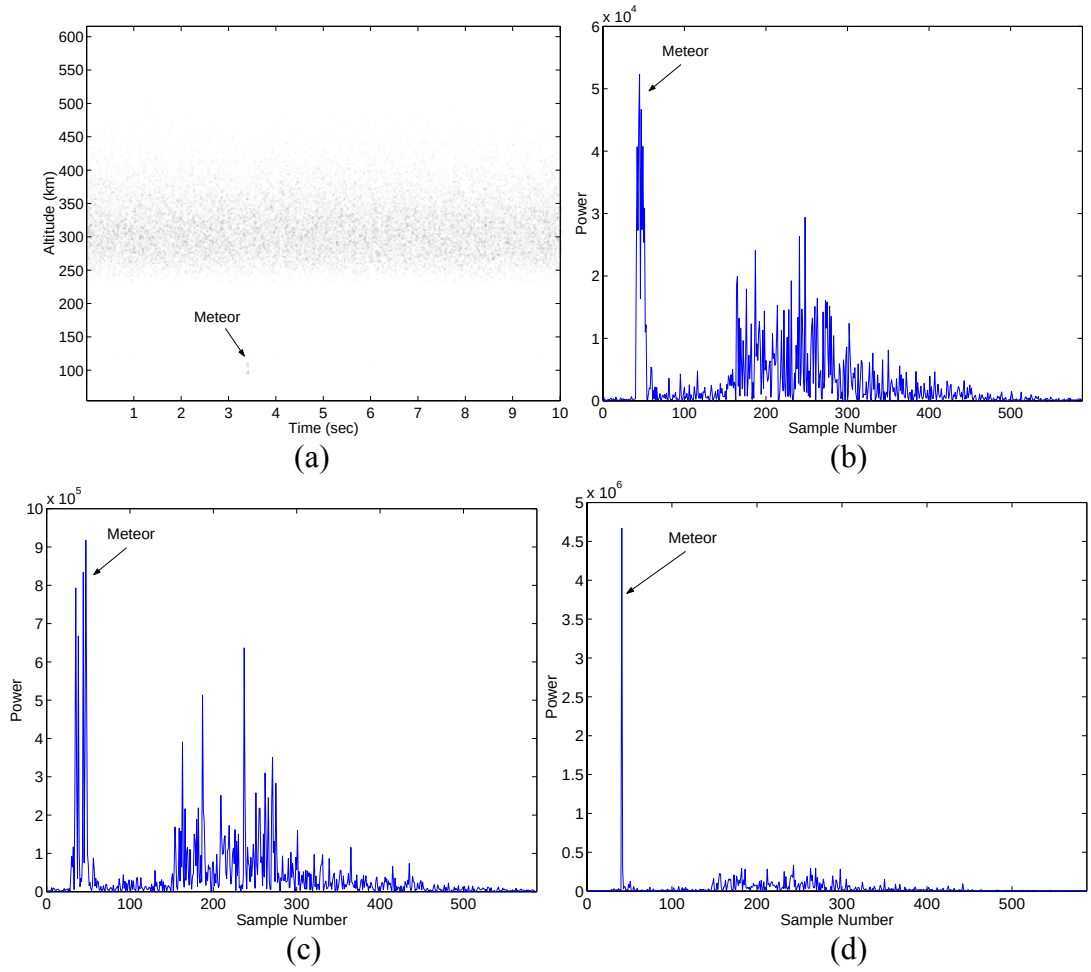

Figure 4.1: Examples of decoding a meteor event (a) Range-Time-Intensity (RTI) plot of 1000 IPPs of decoded ISR data recoded beginning at 22:20:22.990, Sep. 3rd, 2001. Unaveraged power profiles (100 per second) are shown. The E- region appears near 100km altitude while the F-region is above about 230 km altitude. A 13-baud Barker code was transmitted. (b) Power profile of the undocoded meteor event shown in part (a). (c) Power profile of the decoding result of part (b) - incorrect decoding of the Doppler-shifted meteor return spread the meteor return over 26 range-gates. (d) Result of correctly decoding the meteor signal.

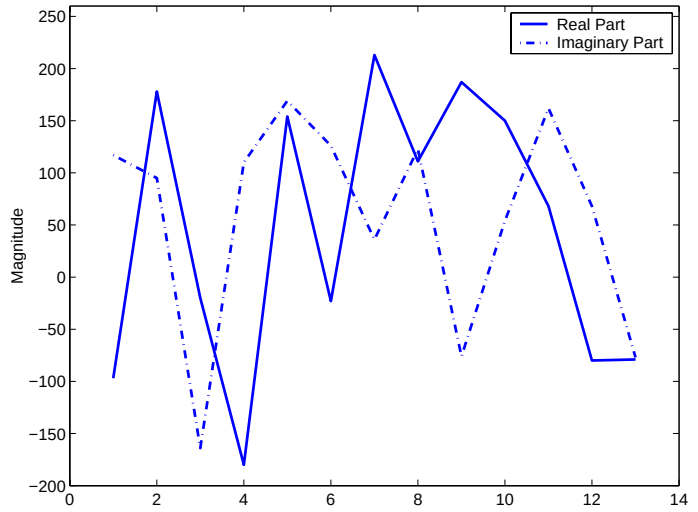

(a)

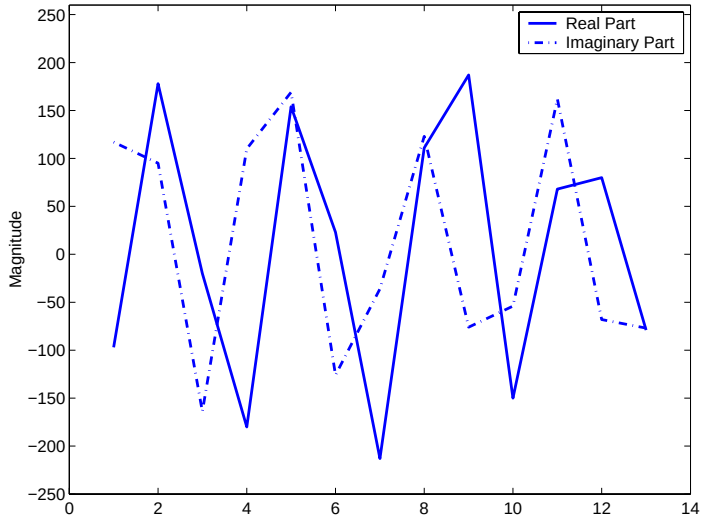

(b)

Figure 4.2: Meteor return signal multiplied by the Barker code (a) The Barker coded meteor signals from Fig. 4.1(a). Solid line is the real part of the complex voltages; dot line is the imaginary part of the complex voltages. (b) The result of the signals in part (a) multiplying the 13 Barker code. We can see the sinusoidal signal here. The frequency corresponds to the speed of the meteor.

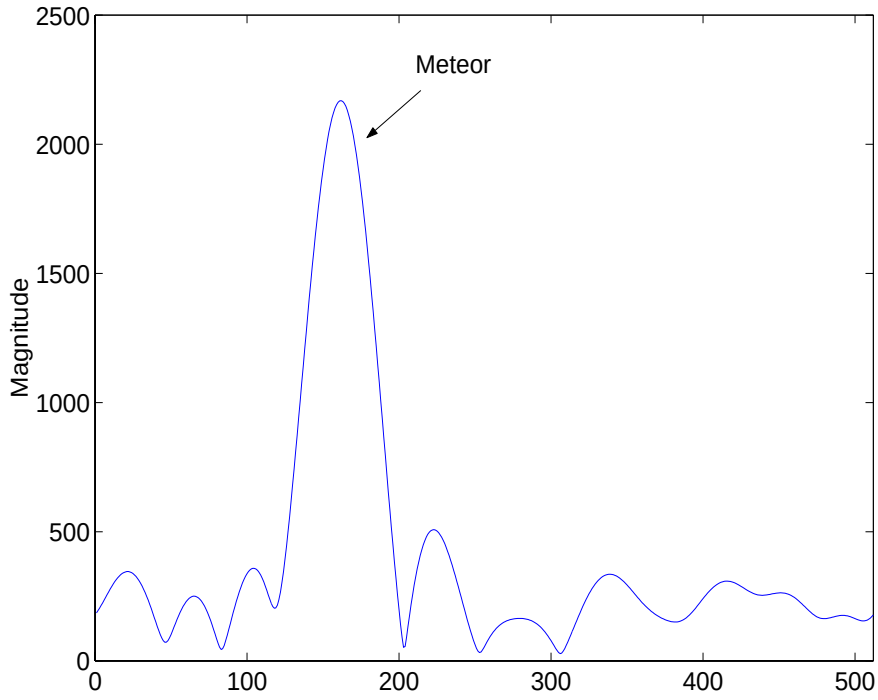

Figure 4.3: Magnitude of the Short Time Fourier Transform (STFT) of the Figure4. 1 meteor event.

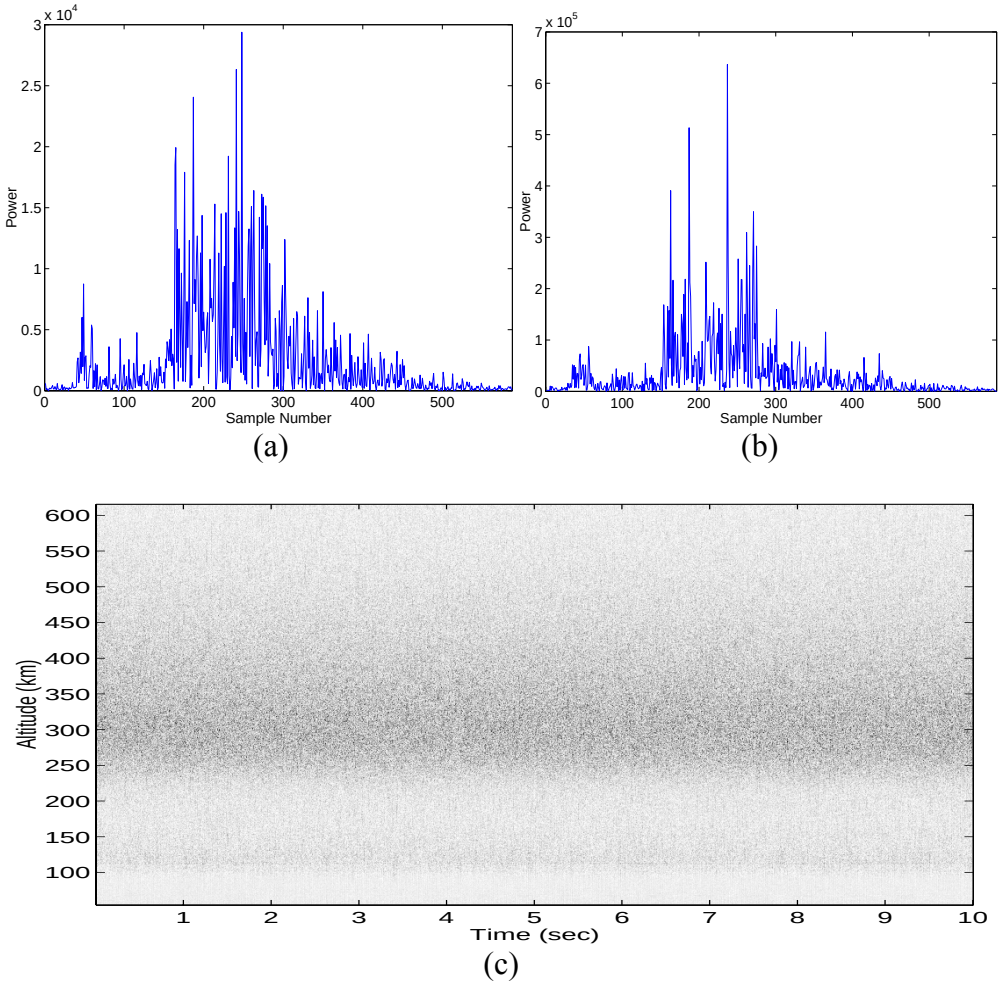

Figure 4.4: Result of the meteor signal removal (a) Power profile of the meteor-event-IPP after meteor removal (undecoded). The power profile of original IPP is shown in Fig. 4.1(b). (b) Power profile after decoding and with the meteor removed. (c) RTI presentation of the Fig. 4.1(a) results with the meteor return removed.

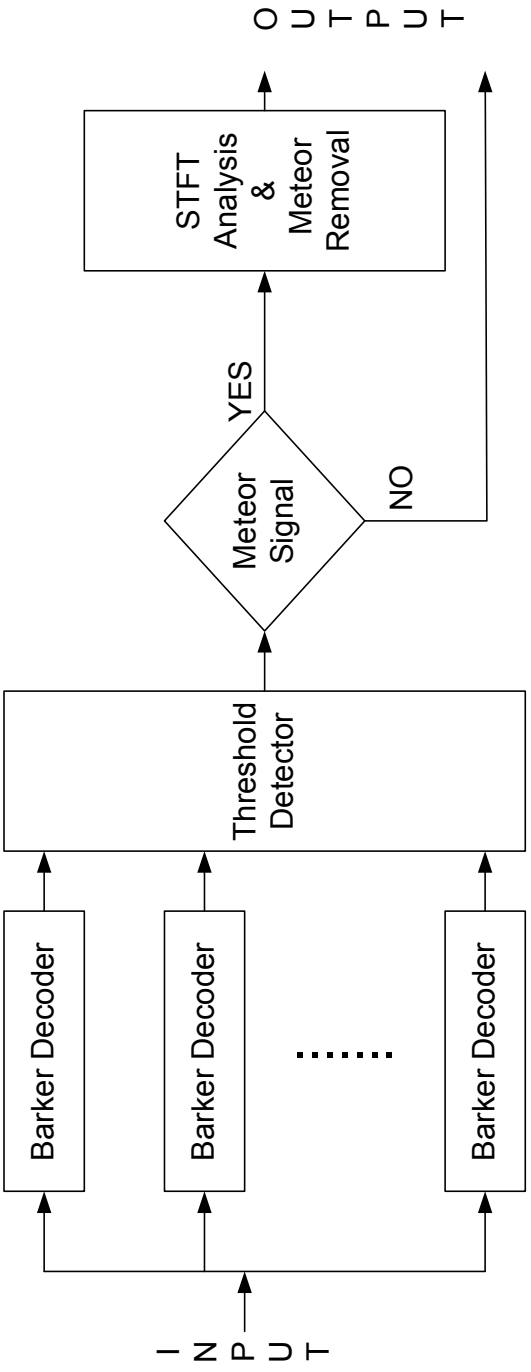

Figure 4.5: Flow chart of the meteor signals detector and removal.

4.2 Interference Removal

The interference observed in AO ISR observation data is very similar to the sparse interference observed in the meteor data. It usually has strong energy and the duration is usually very short. We use this short duration property to design a nonlinear filter to detect and remove the interference. We divide the whole IPP signal into non-overlapping sectors. Each sector has 50 signal samples. We then compare the strongest energy signal sample and the 3rd strongest energy signal sample. If the ratio exceeds certain threshold, we blank the signal sample with strongest energy.

Fig. 4.6 shows the example of the interference removal result. Fig. 4.6 (a) is the original IPP signal recorded at 1:15:27.542 AST, 22 Mar., 2004. Fig. 4.6 (b) is the decoded result of part (a). We can see the interference energy spreads twice the code length which contaminates the result. Fig. 4.6 (c) and (d) are the result of the interference removal and its decoded result, respectively. We can see that the interference signal is removed and there is no contamination of the decoded result. Fig. 4.7 shows the image of the decoded results for 1200 IPPs. The start time of this image is 1:15:25.002 AST, 22 Mar., 2004. Each IPP is 10ms. The interference contaminations are clearly visible here. The arrowheads indicate some of the contaminations. Fig. 4.8 shows the results after interference removal. We can see that the interference contaminations are removed.

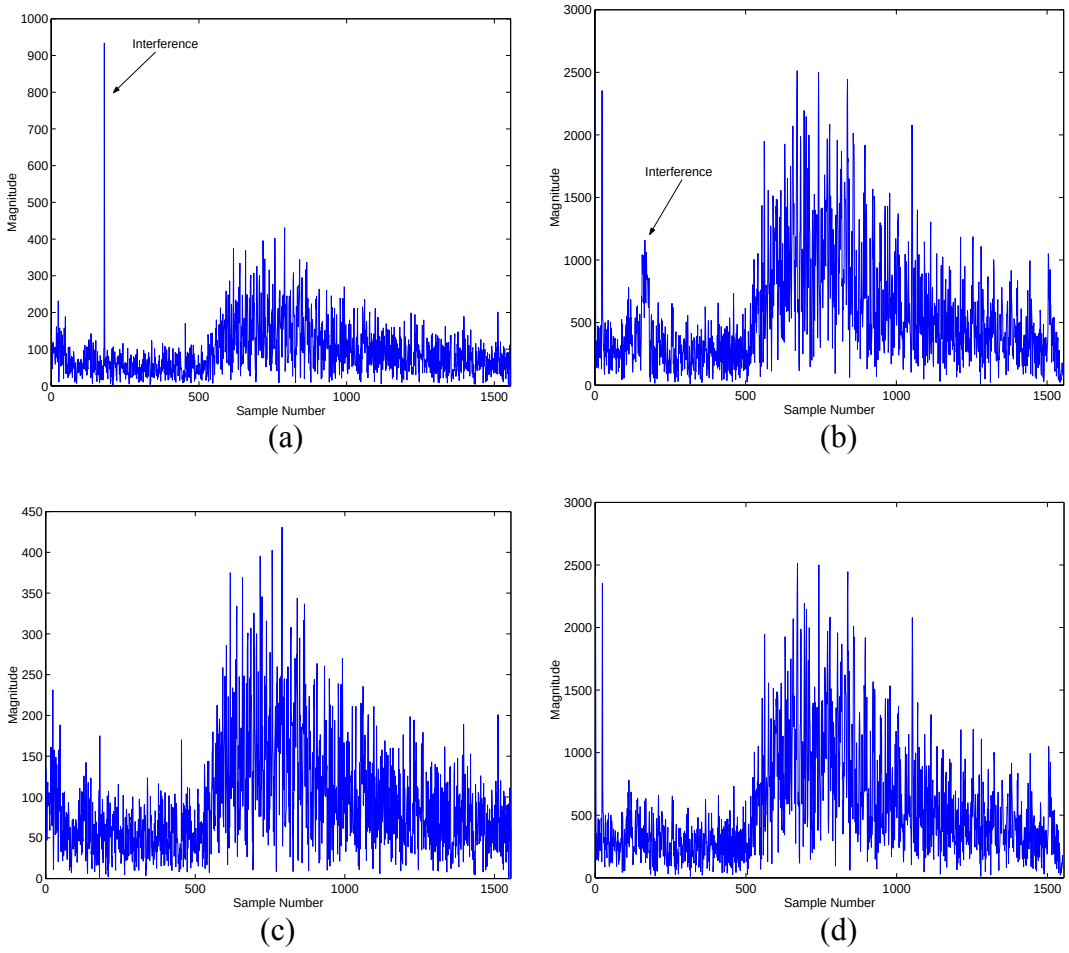

Figure 4.6: The example of the interference removal. (a) The IPP signal recorded at 1:15:27.542 AST 22 Mar. 2004. (b) The decoded result of part (a). (c) The result of the interference removal. (d) The decoded result of part (c).

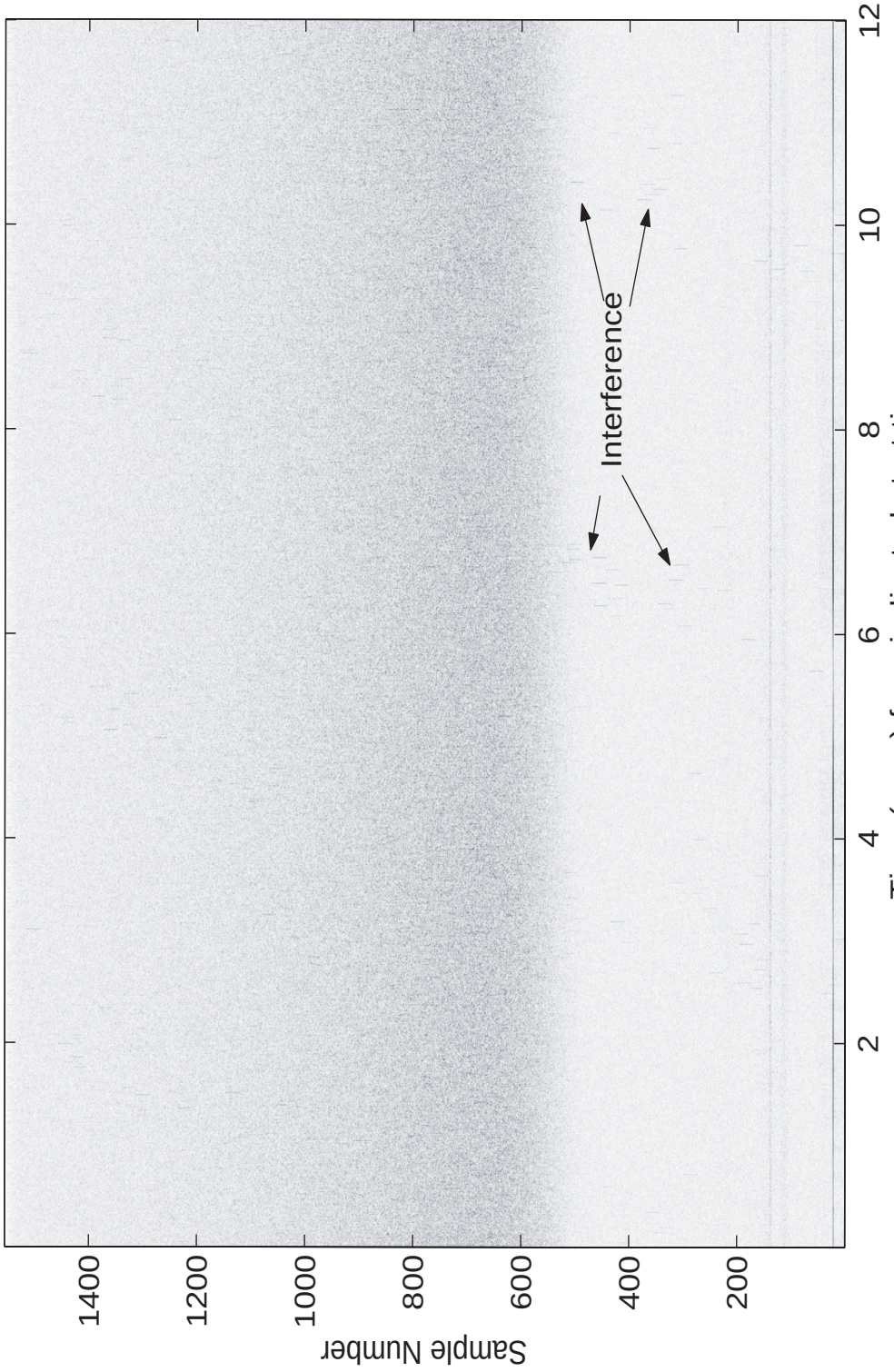

Figure 4.7: The decoded results of 1200 IPPs.

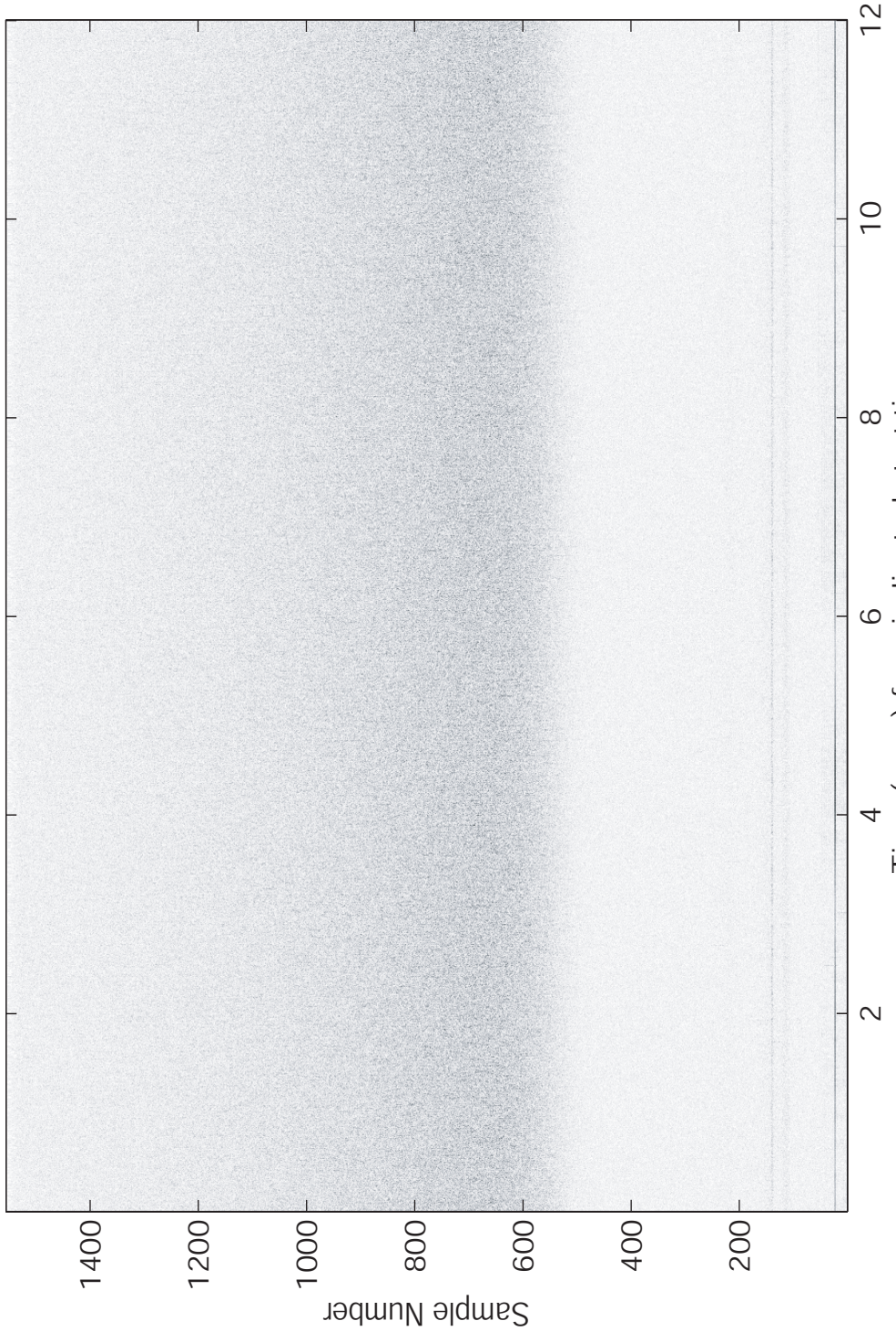

Figure 4.8: The decoded results of 1200 IPPs after interference remobal.

Chapter 5

Other Applications

The meteor observation using the Arecibo Observatory (AO) 430-MHz radar is made by transmitting 45-μs carrier pulses with an interpulse period (IPP) of 1 ms. The return signals are demodulated in in-phase and quadrature-phase channels and sampled at a 1MHz rate. This approach permits the direct observation of the head-echo of the meteor, which is from the scattering by the free electrons surrounding the meteoroid. These meteor head echoes are always seen by the large aperture, high power UHF AO radar. In the contrary the classical meteor trail echoes are rarely seen by the AO radar because the radar scattering cross-section (RCS) of the trail echo is inversely proportional to the radar frequency [6]. Using the filterbank algorithm [5, 8] we have found significant power at low Doppler frequency (near DC) at similar altitude of the meteor head echo for some meteor events. This result suggests that the AO radar can occasionally detect the meteor trail-echo.

The hyper-speed meteor is defined as the speed of the meteor is above 72 km/sec. We modified the meteor return signature algorithm [5, 8] which is used as regular automated meteor searching for the analysis of the meteor observation data from Arecibo Observatory to search for the hyper-speed meteors. We put two consecutive inter-pulse period (IPP) signals together and get the frequency spectrum by the FFT. Then we pass the frequency spectrum through a MRS correlator to detect the presence

of the meteor. We then use short time Fourier transform (STFT) to analyze the possible the hyper-speed events.

5.1 Meteor Trail Echo

We use the filterbank technique described in Section 2.3 to analyze the meteor trail echo. The filterbank consists of 256 filters. The impulse response of each filter is 45-μs sinusoidal wave correlator with different frequency. The range of the frequency is from 0 km/sec to 175 km/sec. The resolution of this filterbank is approximately 0.68 km/sec. Fig. 5.1 shows some filterbank results. Fig. 5.1 (a) is the real part of complex voltages of an IPP signal recorded at 11:48:35.997 AST, 22 February, 2001. Fig. 5.1 (b) shows the low frequency part of the filterbank output of part (a). We can clearly see some power at low Doppler frequency (velocity) form the filterbank output. Fig. 5.1 (c) ~ (f) are the other two examples from IPPs recorded at 12:42:25.076 AST and 15:02:47.445 AST, 22 February, 2001, respectively. We can see that sometimes the power at low Doppler frequency is stronger than the power of the meteor.

5.2 Hyper-Speed Meteor

We modify the MRS detection algorithm described in Section 2.2 to detect the hyper-speed meteor. We use the running window size 2 and ignore the low frequency part (< 72 km/sec) of the frequency spectrum for the detection. We also use lower threshold compared to regular meteor detection. In this way we can detect more weak events but we also have higher false alarm rate.

After detecting the MRS, we then scrutinize the IPP signals. We use a sliding window Short Time Fourier Transform (STFT) technique, described in Section 2.4, to further analyze the two IPP signals. Fig. 5.2 shows some results using this method. The left side plots are the real part of complex voltages. The right side plots are the result of the STFT which yield the maximum peak. We can see sinusoidal signals in the plots, which may suggest the existence of hyper-speed meteor. Note that we have only about half transmitted pulse length signal samples of the sinusoidal wave in Fig. 5.2 (c) from the beginning of the IPP signal, which means we may lose the first half (22 samples) of the return signal. In Fig. 5.2 (e) we have two different frequencies sinusoidal waves. Each of them is about half transmitted pulse length. If the signals are from a hyper-speed meteor, it may suggest the explosion of the meteoroid. The Doppler velocities of the three events shown in Fig. 5.2 are 107.60 km/sec, 72.18 km/sec, and 80.36 km/sec, respectively.

Fig. 5.3 shows an event recorded at 3:36:18.968 AST, 23 February, 2001 and the analysis results. Fig. 5.3 (a) is the real part of the complex voltages of a running window containing 2 IPPs. Fig. 5.3 (b) is the result of the running window FFT. Fig. 5.3 (c) is the output of the MRS correlator. Fig. 5.3 (d) shows the result of the STFT analysis. We can see an unusual peak at high Doppler frequency. But unlike the events shown in Fig. 5.2 we can not see a sinusoidal wave in time domain, shown in Fig. 5.3 (a). This event may suggest the existence of the hyper-speed meteor event.

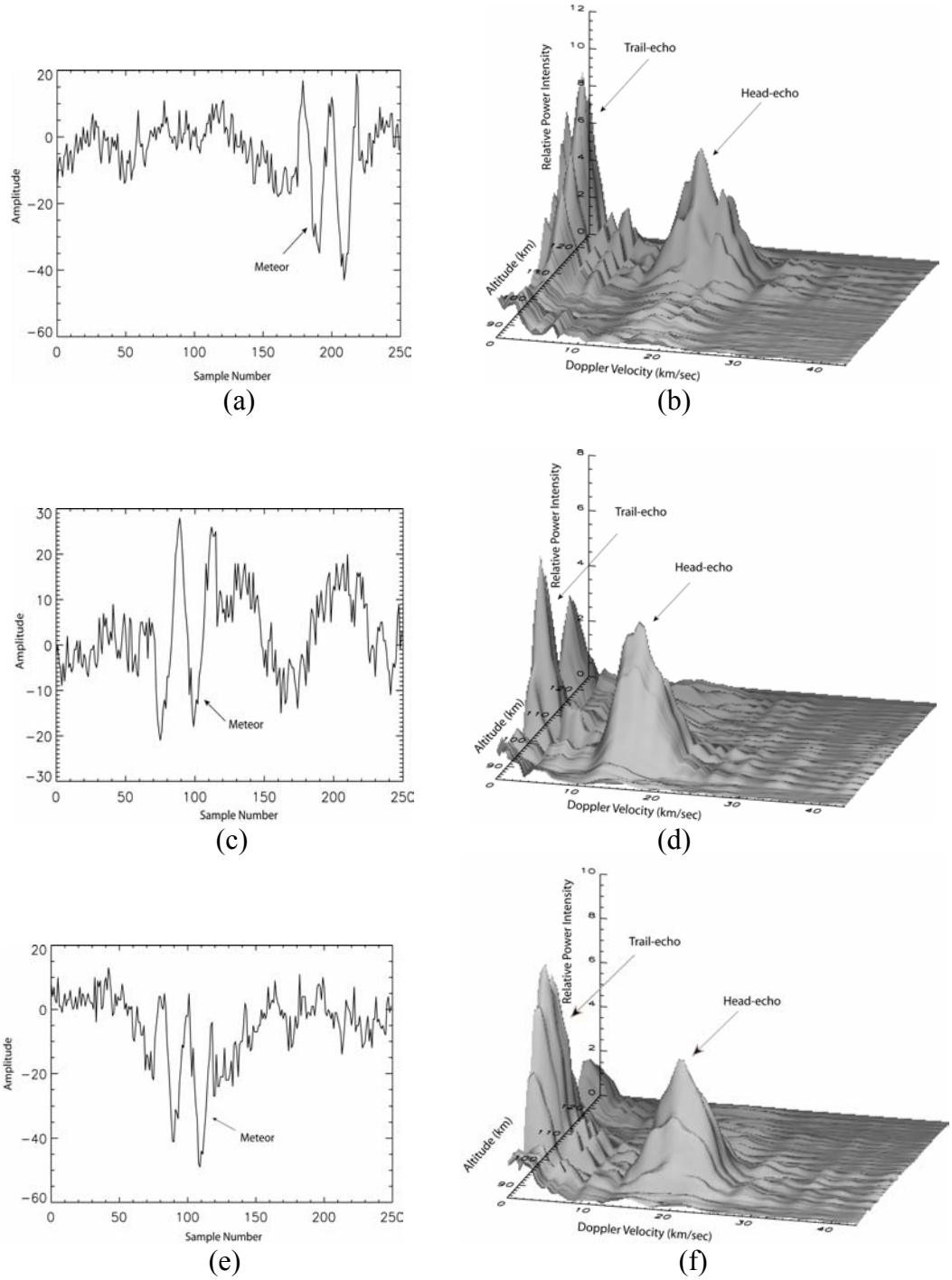

Figure 5.1: The real part of the complex voltage of different meteor events and the results of the filterbank. (a) and (b) are form the meteor event recorded at 11:48:35.997 AST 22 February 2001. (c) and (d) are from the meteor event recorded at 12:42:25.076 AST 22 February 2001. (e) and (f) are from the meteor event recorded at 15:02:47.445 AST 22 February 2001.

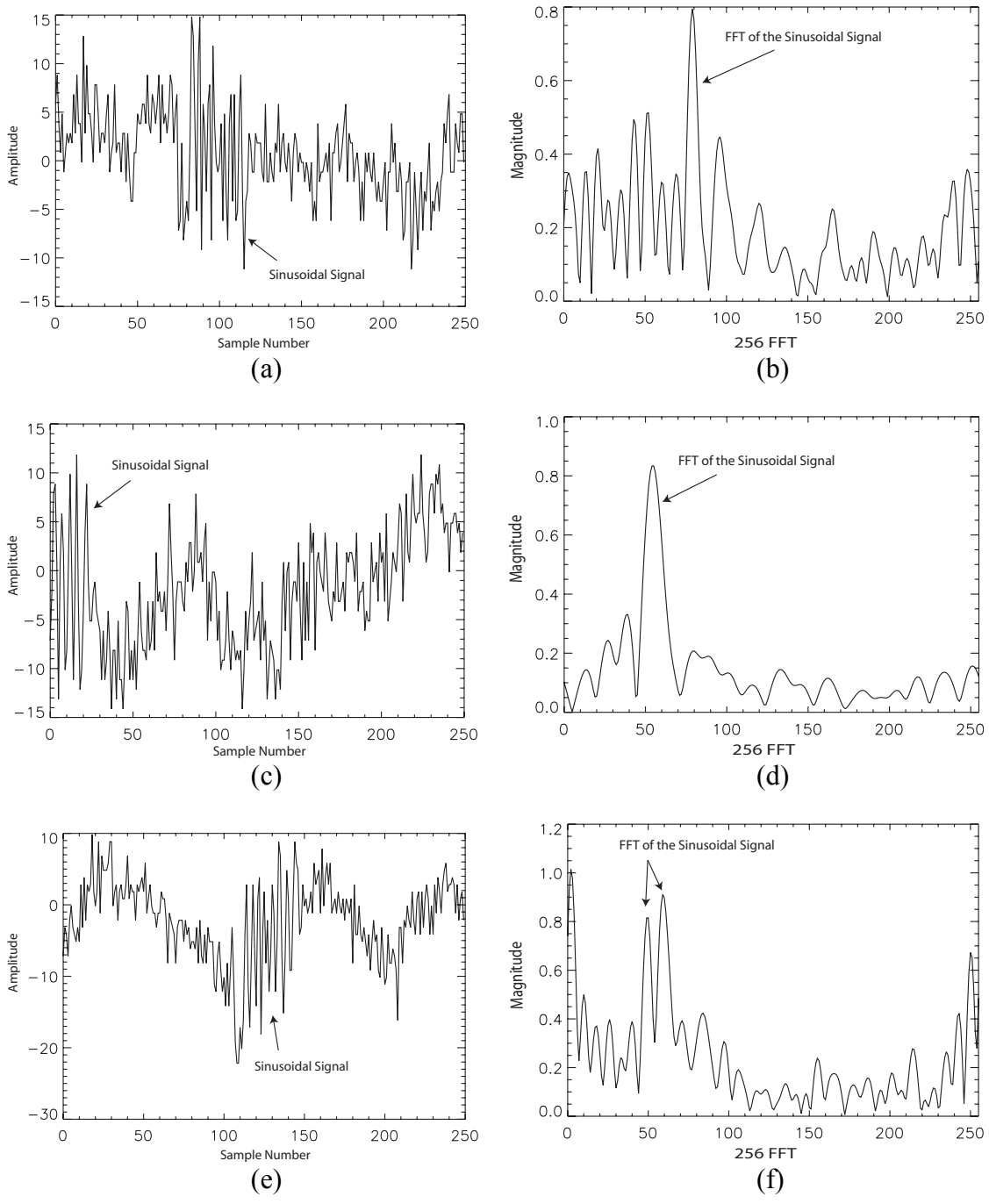

Figure 5.2: The real part of complex voltages of possible hyper-speed meteor events and the results of the STFT analysis. (a) and (b) are recorded at 03:07:24.983 AST 23 February 2001. (c) and (d) are recorded at 20:23:32.198 AST February 2001. (e) and (f) are recorded at 21:26:51.347 AST February 2001.

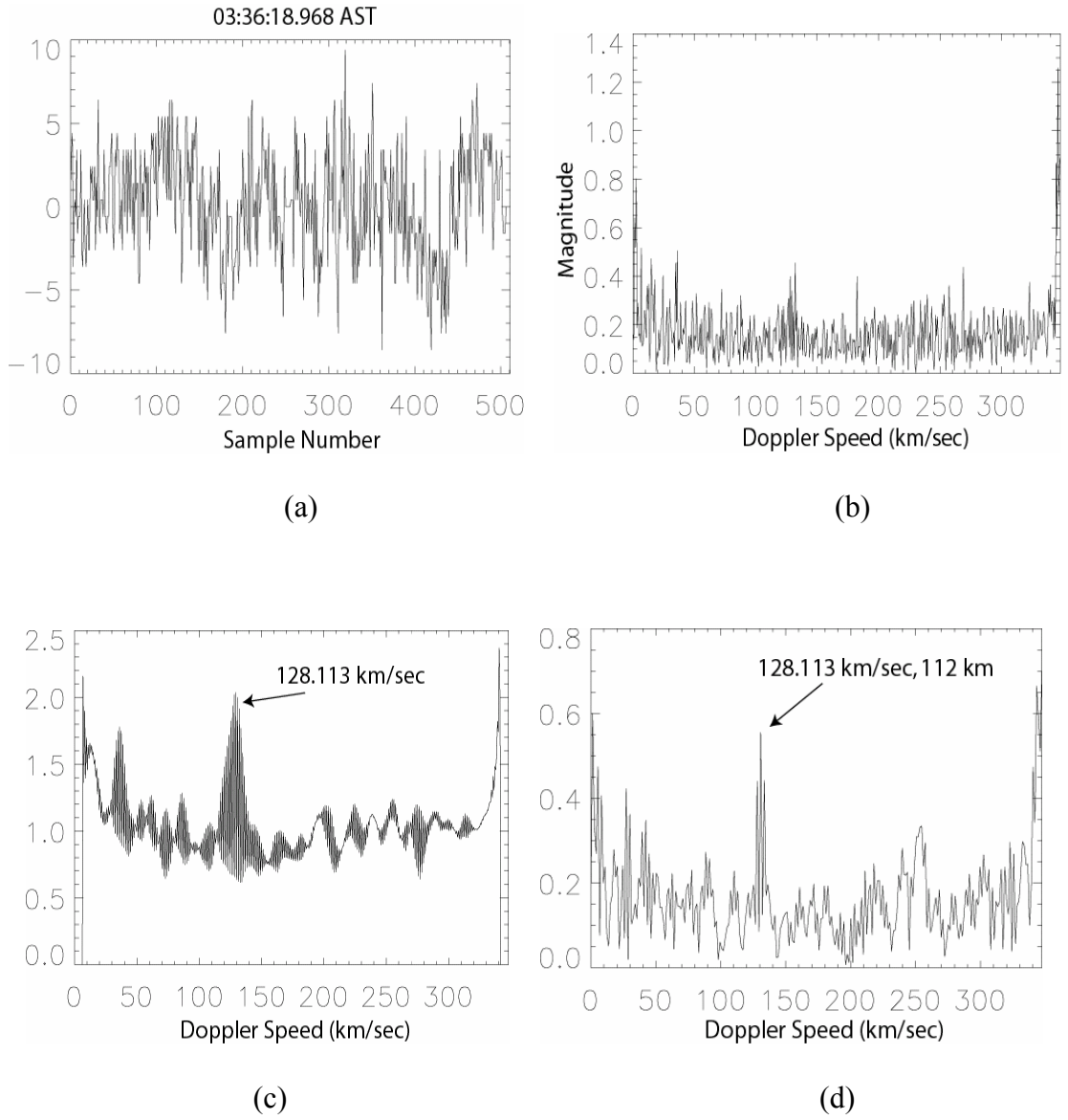

Figure 5.3: One example of weak possible hyper-speed meteor event (a) The real part of the complex voltages of an event (2 IPPs) recorded at 3:36:18.968 AST, 23 February, 2001. (b) The frequency spectrum of part (a). (c) The output of the MRS correlator. (d) The result of the STFT analysis

Chapter 6

Conclusions and Future Work

6.1 Conclusions

In this work we introduce signal processing techniques for interference removal and meteor detection for AO meteor and ISR observation data. For meteor observation data, we present the frequency domain, the time domain, the STFT analysis, and the adaptive filter signal processing techniques to detect the presence of meteor events. We use several IPPs simultaneously, and take the Fast Fourier Transform for frequency domain technique. If a meteor event appears in those IPPs, then we can find a meteor return signature (MRS) in the frequency spectrum. We convolve the frequency spectrum with the special structure to distinguish MRS from noise, and find the estimated Doppler frequency.

For time domain technique, we utilize the prior knowledge of the 45-μs meteor return signal and construct a filterbank containing 256 filters. We pass one IPP through the filterbank to estimate both the Doppler frequency and the altitude of the meteor. Experimental results show that both methods detect meteors very well.

To improve the performance of the frequency domain technique, we use the STFT to further analyze the meteor event. We take 45 signal samples and do the FFT, which reduces the noise level in frequency domain. This technique allows us to detect

weaker meteor events. We also introduce the adaptive filter to remove the incoherent scatter signal, which improves the accuracy of the meteor detection.

We use kurtosis or nonlinear filter method to detect and remove the interference in the meteor observation data. The kurtosis method only works for the sparse interference while nonlinear filter method works for both sparse and dense interference. When the interference and meteor signals occur in the same IPP, the algorithm removes the bursty interference, which makes the meteor detection much easier. Experimental results show the robustness of the algorithm for meteor detection against the interference.

For the ISR observation data, we use a filterbank followed by the short time Fourier transform to remove the meteor signals thus rendering the ionosphere results more accurate. We can also analyze the separated meteor signals to get parameters, such as Doppler frequency (speed) and altitude, after the removal, thus providing two geophysically interesting data streams. We use a nonlinear filter similar to the one introduced for the meteor observation data to remove the interference. We compare the strongest and the 3rd strongest signal samples. If the ration exceeds a certain threshold, we declare a detection of the interference. We then blank the interference signal sample.

6.2 Suggestion for the Future Work

We have proposed several signal processing techniques to solve different problems. For future work, we can apply these techniques to different applications, such as the search of the meteor trail echo and the hyper-speed meteor event. We can also investigate algorithms to save processing time for different techniques, such as

filterbank and STFT analysis, to achieve real time process. We will also continue to invent new techniques and/or improve proposed techniques to get better performance.

References

[1] Q. Zhou, C.A. Tepley, and M. P. Sulzer, "Meteor observations by the Arecibo 430 MHz incoherent scatter radar I. Detection, statistics, and interpretation," *Journal of Atmospheric and Terrestrial Physics* 57, pp. 412-431, 1995

[2] J. D. Mathews, D. D. Meisel, K. P. Hunter, V. S. Getman, and Q. Zhou, "Very high resolution studies of micrometeors using the Arecibo 430 MHz radar," *Icarus* 126, pp. 157-169, 1997

[3] Q. Zhou, P. Perillat, J. Y. N. Cho, and J. D. Mathews, "Simultaneous meteor echo observations by large aperture VHF and UHF radars," *Radio Science* 33, pp. 1641-1654, 1998

[4] D. Janches, J. D. Mathews, D. D. Meisel, V. S. Getman, and Q.-H. Zhou, "Doppler studies of near-antapex UHF radar micrometeors," *Icarus* 143, pp. 347-253, 2000

[5] J. D. Mathews, J. F. Doherty, C.-H. Wen, S. J. Briczinski, D. Janches, D. D. Meisel, "An update of UHF radar meteor observations and associated signal processing techniques at Arecibo Observatory," *Journal of Atmospheric and Solar-Terrestrial Physics*, Vol. 65, pp. 1139-1149, July 2003.

[6] J. D. Mathews, "Radio science issues surrounding HF/VHF/UHF radar meteor studies," *Journal of Atmospheric and Solar-Terrestrial Physics,* Vol. 66, pp. 285-299, 2004.

[7] D. Janches, D. D. Meisel, J. D. Mathews, "Orbital properties of the Arecio micrometeoroids at earth intersection," *Icarus* 150, pp. 206-218, 2001

[8] C.-H. Wen, J. F. Doherty, J. D. Mathews, "Time-frequency radar processing for meteor detection," *IEEE Trans. Geosci. Remote Sensing*, *IEEE Trans*., Vol. 42, Issue 3, 501-510, 2004.

[9] C.-H. Wen, J. F. Doherty, J. D. Mathews, D. Janches, "Meteor detection and non-periodic bursty interference removal for Arecibo data," *Journal of Atmospheric and Solar-Terrestrial Physics,* Vol. 67, pp. 275-281, February 2005

[10] J. F. Rowe, "Downward transport of nighttime E_s-layers into the E-region ar Arecibo", *Journal of Atmospheric and Solar Terrestrial Physics* 36, pp. 225-235, 1974.

[11] K. L. Miller and L. G. Smith, "Horizontal structure of midlatitude sporadic E layers observed by incoherent scatter radar", *Radio Science* 10, 271-276, 1975.

[12] J. D. Mathews and F. S. Bekeny, "Upper atmosphere tides and the vertical motion of ionospheric sporadic layers at Arecibo," *Journal of Geophysical Research* 84, 2743-2750, 1979.

[13] J. D. Mathews, Y. T. Morton, and Q. Zhou, "Observations of ion layer motions during the AIDA campaign," *J. Atmos. Terr. Phys*., 55, 447-457, 1993.

[14] J. D. Mathews, M. P. Sulzer and P. Perillat, "Aspects of layer electrodynamics inferred from high-resolution ISR observations of the 80-270 km ionosphere," Geophysical Research Letters, 24, 1411-1414, 1997.

[15] M. P. Sulzer, "Meteor Science from Regular Incoherent Scatter Radar Ionospheric Observations at Arecibo," *Atmos. Chem. Phys. Discuss*., 4, 805-831, 2004.

[16] J. L. Chau, Woodman, R. F, "Observations of Meteor-Head Echoes Using the Jicamarca 50 MHz Radar in Interferometer Mode," *Atmos. Chem. Phys*., 4, 511-521, 2003.

[17] John G. Proakis, *Digital Communications*, 4th edition, McGraw-Hill, 2001

[18] Athanasios Papoulis, *Probability, Random Variables, and Stochastic Processes*, 3rd edition, McGraw-Hill, 1991.

[19] Simon Haykin, *Adaptive Filter Theory*, 4th edition, Prentice Hall, 2002.

Vita

Chun-Hsien Wen was born in Tainan, Taiwan in July 1974. In June 1996 he received the B. Eng. Degree in Electrical Engineering from National Tsing Hua University, Hsinchu, Taiwan. From August 1999 to December 2001, he was a master student in the Department of Electrical Engineering, the Pennsylvania State University, University Park, Pennsylvania, USA. In January 2002, after getting his master's degree, he became a Ph.D. student and research assistant in the Department of Electrical Engineering, the Pennsylvania State University, University Park, Pennsylvania, USA and has worked on his doctoral degree since then.

His research interests include wireless communication, statistical signal processing, etc.